UNIVERSITÉ DU QUÉBEC

MÉMOIRE PRÉSENTÉ À
L'UNIVERSITÉ DU QUÉBEC À TROIS-RIVIÈRES

COMME EXIGENCE PARTIELLE DE LA
MAÎTRISE EN SCIENCE DE L'ÉNERGIE ET DES MATÉRIAUX
OFFERT EN EXTENSION PAR L'INSTITUT NATIONAL DE LA
RECHERCHE SCIENTIFIQUE

PAR
ROSA BEIG AGHA

CARBON NANOSTRUCTURES: PRODUCTION AND CHARACTERIZATION

SEPTEMBRE 2010

Résumé étendu en Français

La technologie de la pile à combustible à membrane électrolytique polymère (PEMFC – *Polymer Electrolyte Membrane Fuel Cell*) a fait des progrès rapides dans les dernières années. Un secteur actif se penche sur l'amélioration de la performance à long terme de catalyseurs à support de carbone, ce qui a été reconnu comme un des problèmes les plus importants à résoudre pour la mise en marché des PEMFCs. La partie centrale d'une PEMFC est l'assemblage membrane-électrode (MEA), qui est composé de deux électrodes (anode et cathode) et d'une membrane échangeuse de cations. Ces électrodes sont en général fabriquées de noir de charbon (le plus souvent du Vulcan XC-72) sur un support de papier carbone ou de tissu carbone.

Les couches de catalyseur (CL – *Catalyst Layer*) faisant partie des électrodes sont l'endroit où ont lieu les réactions électrochimiques et sont composées d'un catalyseur (Pt ou alliage de Pt) supporté par du noir de charbon et de ionomères pour la conduction protonique. Comme mentionnée ci-haut, la durabilité de ces CLs est le problème crucial pour le développement et la mise en marché des PEMFCs.

Malgré son utilisation répandue, le noir de charbon est sujet à une oxydation électrochimique par des oxydes de surface et éventuellement se transforme en CO_2 à la cathode d'une pile à combustible où il est sujet à des hauts degrés d'acidité, de tension, de température et d'humidité. Au fur et à mesure que le carbone est oxydé, les nanoparticules métalliques du catalyseur seront perdues de l'électrode ou s'agglomèreront en particules plus grandes. L'oxydation du support de carbone peut aussi mener à des changements d'hydrophobicité superficielle qui peut mener à des difficultés de transport des gaz.

Plusieurs groupes de recherche ont proposé qu'un carbone avec un plus grand degré de graphitisation puisse être plus résistant à la corrosion dans le voisinage cathodique. De plus, un carbone avec une porosité accrue, c'est-à-dire avec un plus grand volume de pores et donc ayant une microporosité accrue, aurait comme effet de mieux évacuer l'eau liquide produite à la cathode d'une PEMFC.

L'objectif de ce mémoire est de préparer et de caractériser des nanostructures de carbone (CNS – *Carbon Nanostructures*, en licence à l'Institut de recherche sur l'hydrogène, Québec, Canada), un carbone avec un plus grand degré de graphitisation et une meilleure porosité. Le Chapitre 1 est une description générale des PEMFCs et plus particulièrement des CNS comme support de catalyseurs, leur synthèse et purification. Le Chapitre 2 décrit plus en détails la méthode de synthèse et la purification des CNS, la théorie de formation des nanostructures et les différentes techniques de caractérisation que nous avons utilisés telles que la diffraction aux rayons-X (XRD – *X-ray diffraction*), la microscopie électronique à transmission (TEM – *transmission electron microscope*), la spectroscopie Raman, les isothermes d'adsorption d'azote à 77 K (analyse BET, t-plot, DFT), l'intrusion au mercure, et l'analyse thermogravimétrique (TGA – *thermogravimetric analysis*). Le Chapitre 3 présente les résultats obtenus à chaque étape de la synthèse des CNS et avec des échantillons produits à l'aide d'un broyeur de type SPEX® (SPEX/CertiPrep 8000D) et d'un broyeur de type planétaire (Fritsch Pulverisette 5). La différence essentielle entre ces deux types de broyeur est la façon avec laquelle les matériaux sont broyés. Le broyeur de type SPEX secoue le creuset contenant les matériaux et des billes d'acier selon 3 axes produisant ainsi des impacts de très grande énergie. Le broyeur planétaire quant à lui fait tourner et déplace le creuset contenant les matériaux et des billes d'acier selon 2 axes (plan). Les matériaux sont donc broyés différemment et l'objectif est de voir si les CNS produits ont les mêmes structures et propriétés.

Lors de nos travaux nous avons été confrontés à un problème majeur. Nous n'arrivions pas à reproduire les CNS dont la méthode de synthèse a originellement été développée dans les laboratoires de l'Institut de recherche sur l'hydrogène (IRH). Nos échantillons présentaient toujours une grande quantité de carbure de fer au détriment de la formation de nanostructures de carbone. Après plusieurs mois de recherche nous avons constaté que les métaux de base, soit le fer et le cobalt, étaient contaminés. Néanmoins, ces recherches nous ont enseigné beaucoup et les résultats sont présentés aux Appendices I à III.

Le carbone de départ est du charbon activé commercial (CNS201) qui a été préalablement chauffé à 1,000 °C sous vide pendant 90 minutes pour se débarrasser de toute humidité et

autres impuretés. En première étape, dans un creuset d'acier durci du CNS201 prétraité fut mélangé à une certaine quantité de Fe et de Co (99.9 % purs). Des proportions typiques sont 50 pd. %, 44 pd. %, et 6 pd. % pour le C, le Fe, et le Co respectivement. Pour les échantillons préparés avec le broyeur SPEX, trois à six billes en acier durci furent utilisées pour le broyage, de masse relative échantillon/poudre de 35 à 1. Pour les échantillons préparés avec le broyeur planétaire, trente-six billes en acier durci furent utilisées pour le broyage, de masse relative échantillon/poudre de 10 à 1. L'hydrogène fut alors introduit dans le creuset pour les deux types de broyeur à une pression de 1.4 MPa, et l'échantillon fut broyé pendant 12 h pour le SPEX et 24 h pour le planétaire. Le broyeur SPEX a un rendement de transfert d'énergie mécanique plus grand qu'un broyeur planétaire, mais il a le désavantage de contaminer davantage l'échantillon en Fe par attrition. Cependant, ceci peut être négligé vu que le Fe était un des catalyseurs métalliques ajoutés au creuset. En deuxième étape, l'échantillon broyé est transféré sous gaz inerte (argon) dans un tube en quartz, qui est alors chauffé à 700 °C pendant 90 minutes.

Des mesures de patrons de diffraction à rayons-X sur poudre furent faites pour caractériser les changements structurels des CNS lors des étapes de synthèse. Ces mesures furent prises avec un diffractomètre Bruker D8 FOCUS utilisant le rayonnement Cu Kα (λ = 1.54054 Å) et une géométrie Thêta/2Thêta. La Figure 3.1 montre le patron de diffraction de rayon-X du charbon activé utilisé comme précurseur pour produire les CNS. Le charbon activé est préchauffé à haute température (1,000 °C) pendant 1 h pour enlever l'humidité. La Figure 3.2 montre les patrons de diffraction de rayons-X des échantillons SPEX et planétaire après broyage de 12 h et 24 h, respectivement. Les structures de charbon ne sont pas encore bien définies, mais un pic à $2\theta \approx 20°\text{-}30°$ correspond aux petites cristallites à caractère turbostatique et un pic correspondant au fer et au carbure de fer apparaît à $2\theta \approx 45°$.

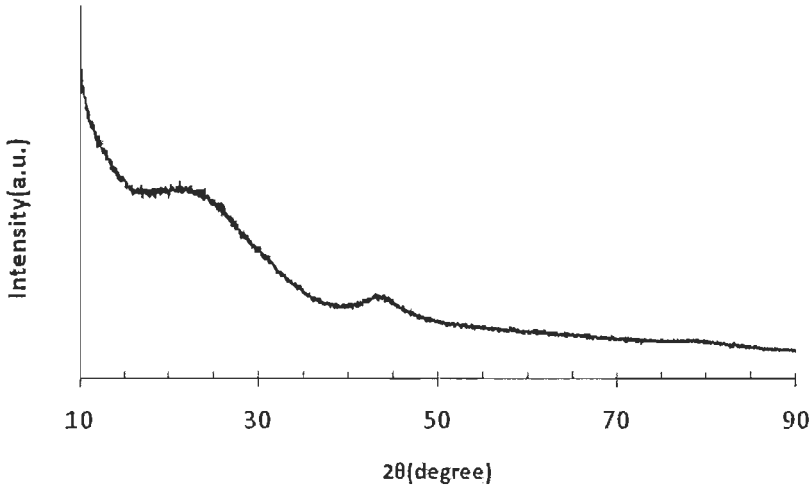

Figure 3.1 : Patron XRD du charbon activé

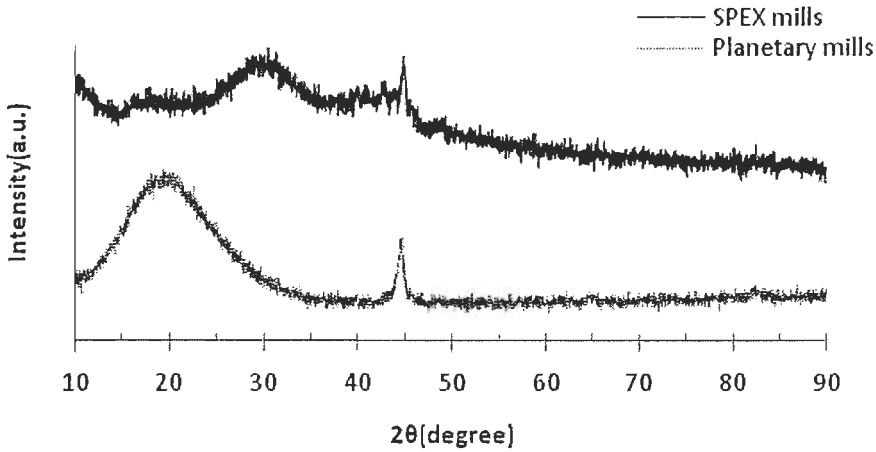

Figure 3.2 : Patrons XRD des échantillons SPEX et planétaire après broyage de 12 h et 24 h, respectivement.

La Figure 3.3 montre les patrons de diffraction de rayons-X des échantillons broyés SPEX et planétaire après chauffage à 700 °C pendant 1.5 h sous argon. Le pic à $2\theta \approx 26.5^{\circ}$ correspond au graphite cristallin (002) et les pics à $2\theta \approx 44.7^{\circ}$, 65.0° and 82.3°, correspondent au fer et au cobalt.

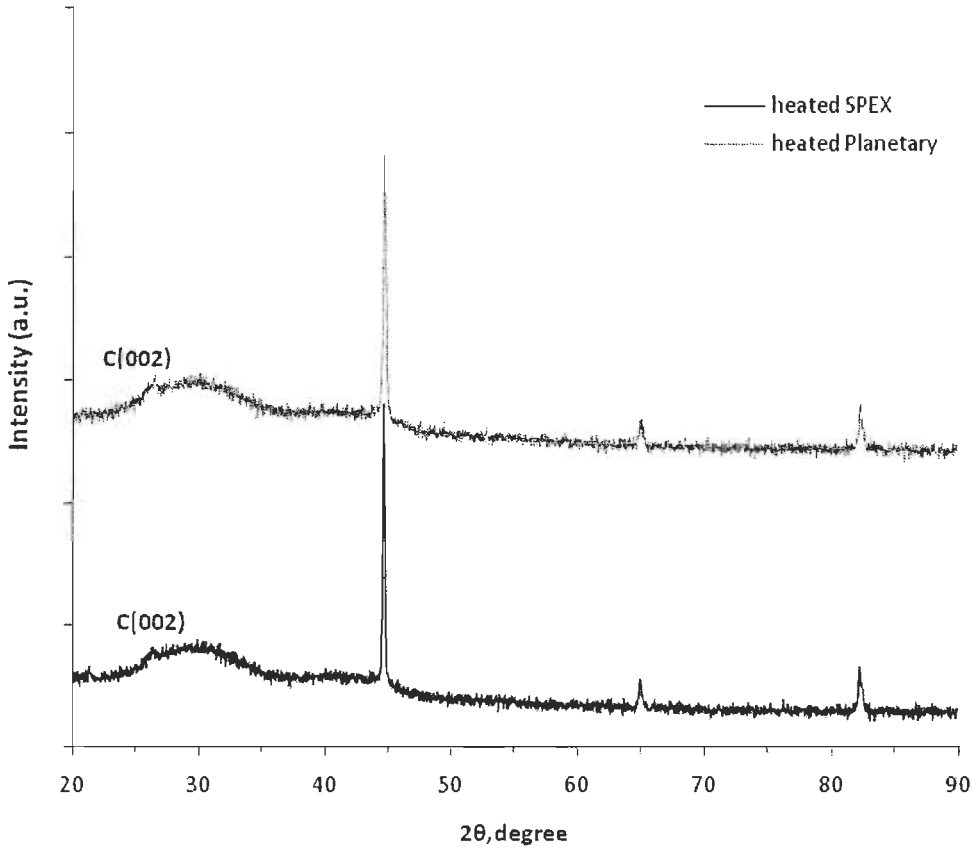

Figure 3.3 : Patrons XRD des échantillons broyés SPEX et planétaire après chauffage sous argon.

La Figure 3.4 montre les patrons de diffraction de rayons-X des échantillons SPEX et planétaire broyés et chauffés et après purification dans une solution ultrasoniquée de HCl 6 M pendant 3 h. Le pic principal et bien défini correspond au graphite cristallin à $2\theta \approx 26.37^{\circ}$ (d_{002} = 3.37 Å) et $2\theta \approx 26.25^{\circ}$ (d_{002}=3.39 Å) pour les échantillons SPEX et planétaire, respectivement. Les autres pics de moindre intensité indiquent encore une présence du fer et du cobalt.

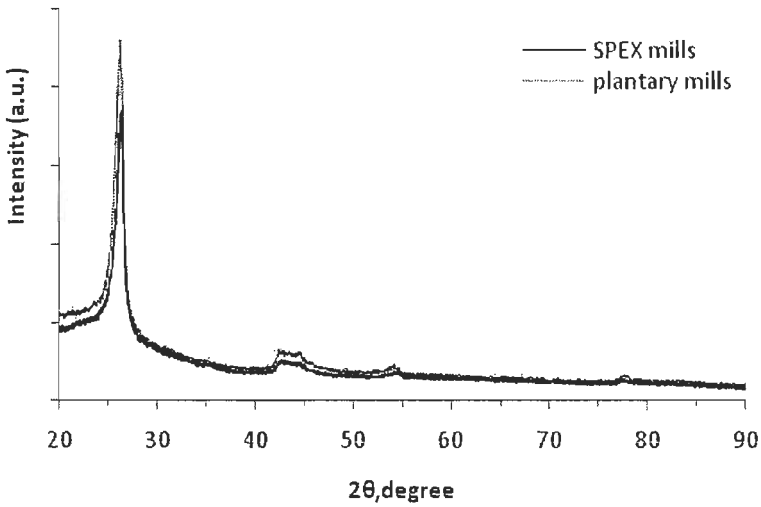

Figure 3.4 : Patrons XRD des échantillons SPEX et planétaire après purification au HCl pendant 3 h.

Les Figures 3.5 à 3.9 sont des images TEM montrant les CNS d'un échantillon planétaire tandis que les Figures 3.10 à 3.13 sont des images TEM montrant les CNS d'un échantillon SPEX. Ces images montrent des CNS dont les formes ressemblent à des rubans ayant des diamètres allant de 40 à 130 nm et des agglomérats de carbone amorphe. Quelques nanoparticules de fer d'environ 26 nm de diamètre sont aussi visibles.

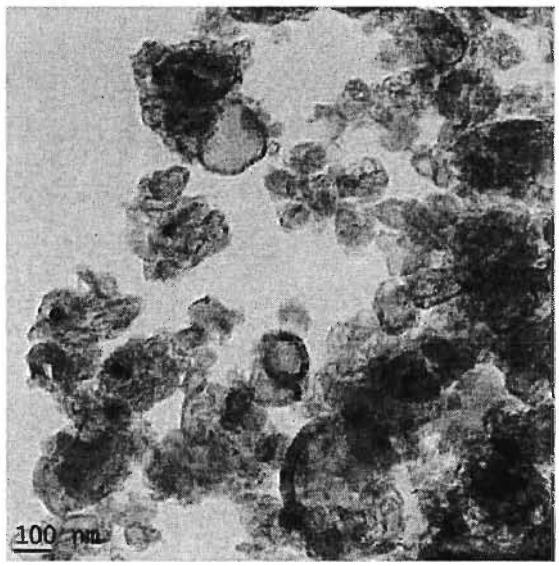

Figure 3.5 : Image TEM d'un échantillon planétaire purifié (broyé pendant 24 h et chauffé à 700 °C pendant 90 minutes).

La Figure 3.6 montre des rubans nanographitiques formé des plans de graphite bien ordonnés d'une épaisseur d'environ 14 nm et dont l'espacement d_{200} est moins que 1 nm.

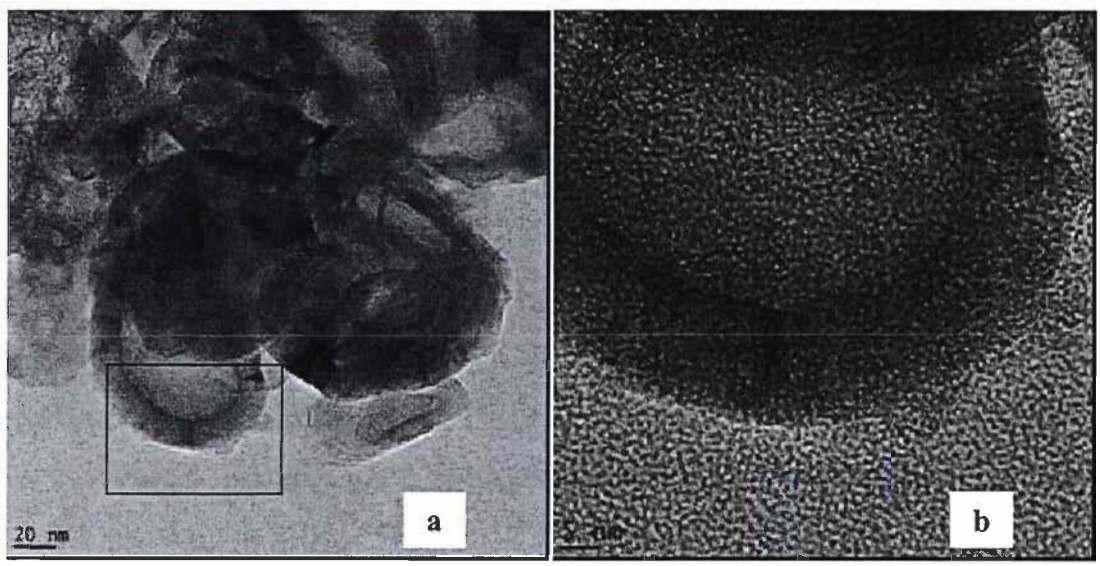

Figure 3.6 : (a) Images TEM d'un échantillon planétaire purifié. (b) Agrandissement de la portion d'image dans le rectangle de l'image (a).

La Figure 3.7 montre des défauts dans les plans graphitiques indiquant que les rubans de CNS on une structure turbostratique avec 3.38 Å < d_{200} < 3.44 Å.

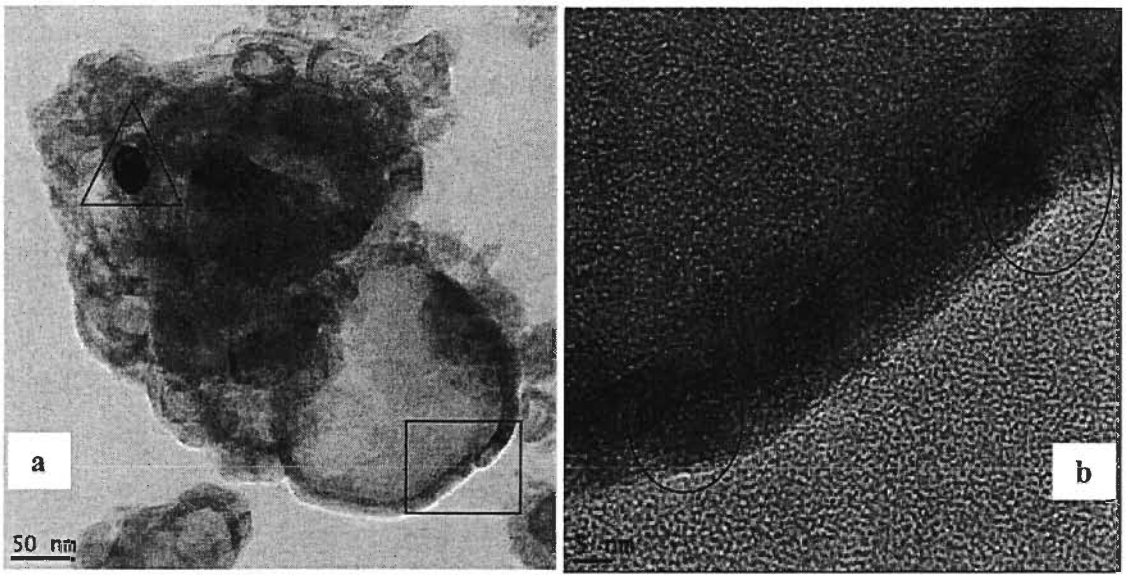

Figure 3.7 : (a) Images TEM d'un échantillon planétaire purifié. (b) Agrandissement de la portion d'image dans le rectangle de l'image (a).

La Figure 3-8 est un agrandissement du triangle de la Figure 3-7(a) où on peut voir une nanoparticule de fer entourée de feuilles graphitiques. Lors de traitement additionnel à l'acide, les feuilles sont exfoliées de la surface et forment des rubans.

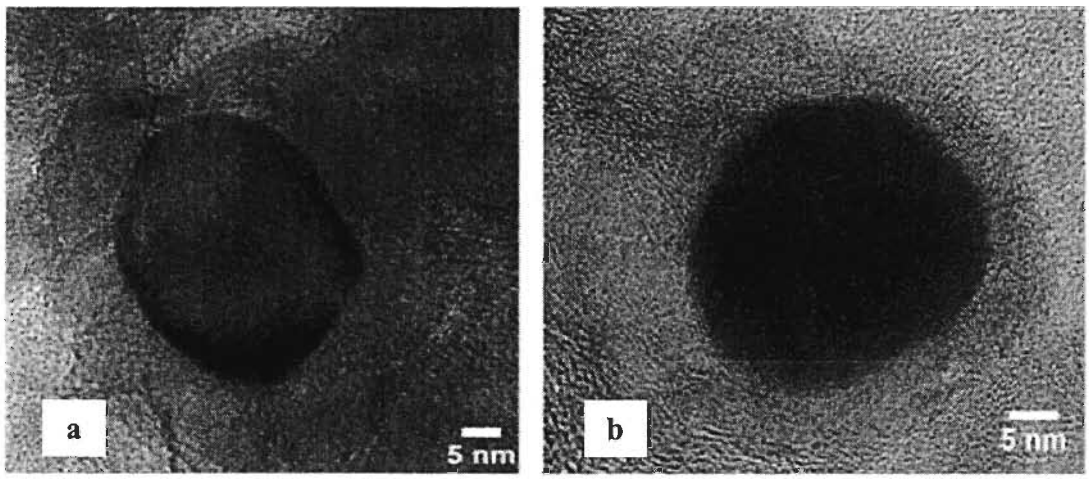

Figure 3.8 : (a) et (b) Images TEM de deux nanoparticules de fer entourées par des plans graphitiques.

La Figure 3.9 montre la présence de rubans graphitiques et d'un agglomérat de carbone amorphe.

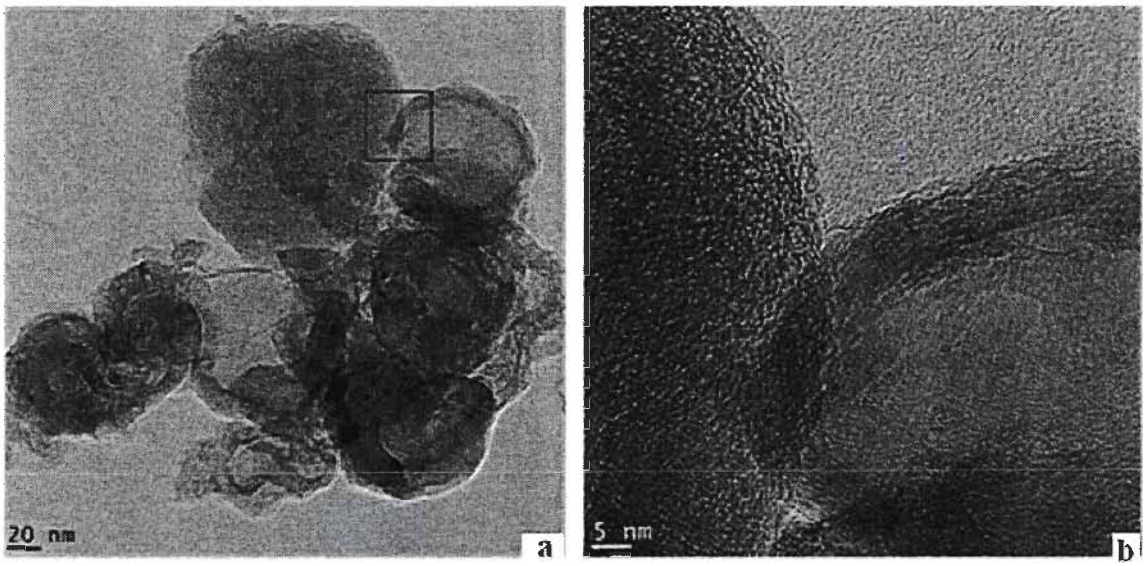

Figure 3.9 : (a) Images TEM de rubans nano graphitiques et de carbone amorphe. (b) Agrandissement de la portion d'image dans le rectangle de l'image (a).

Les Figures 3.10 à 3.13 sont les images TEM d'un échantillon SPEX et montrent essentiellement les mêmes structures que les échantillons planétaires.

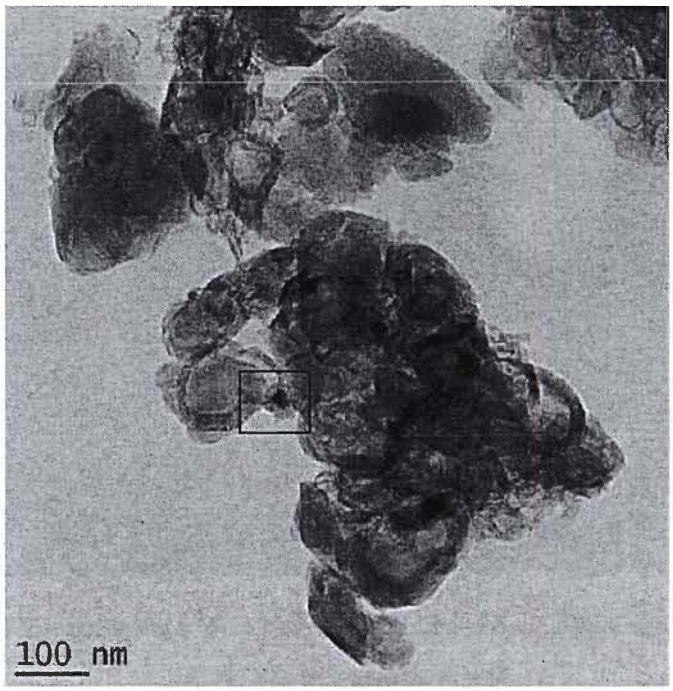

Figure 3.10 : Image TEM d'un échantillon SPEX purifié (broyé pendant 12 h et chauffé à 700 °C pendant 90 minutes). La portion d'image dans le rectangle correspond à une nanoparticule de fer (diamètre de 21 nm) entourée par des plans graphitiques.

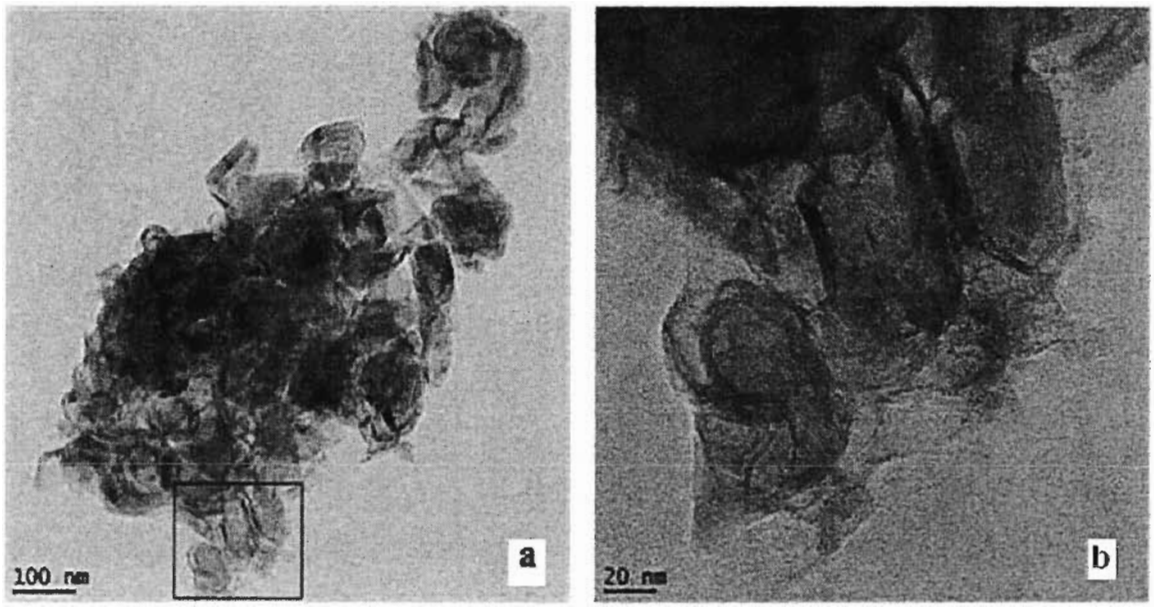

Figure 3.11 : (a) Images TEM d'un échantillon SPEX purifié. (b) Agrandissement de la portion d'image dans le rectangle de l'image (a).

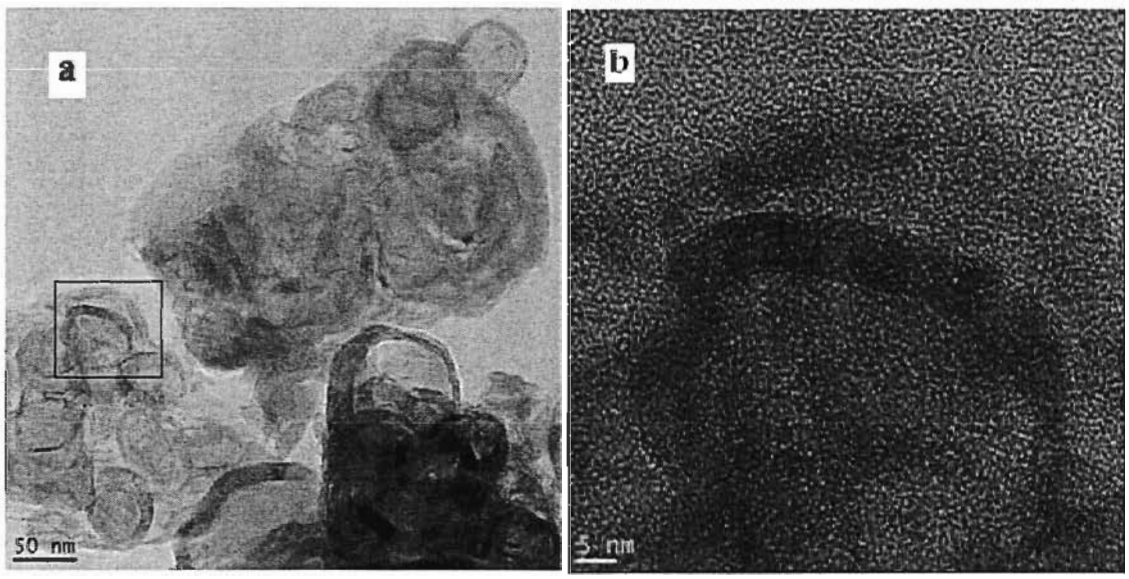

Figure 3.12 : (a) Images TEM d'un échantillon SPEX purifié. (b) Agrandissement de la portion d'image dans le rectangle de l'image (a).

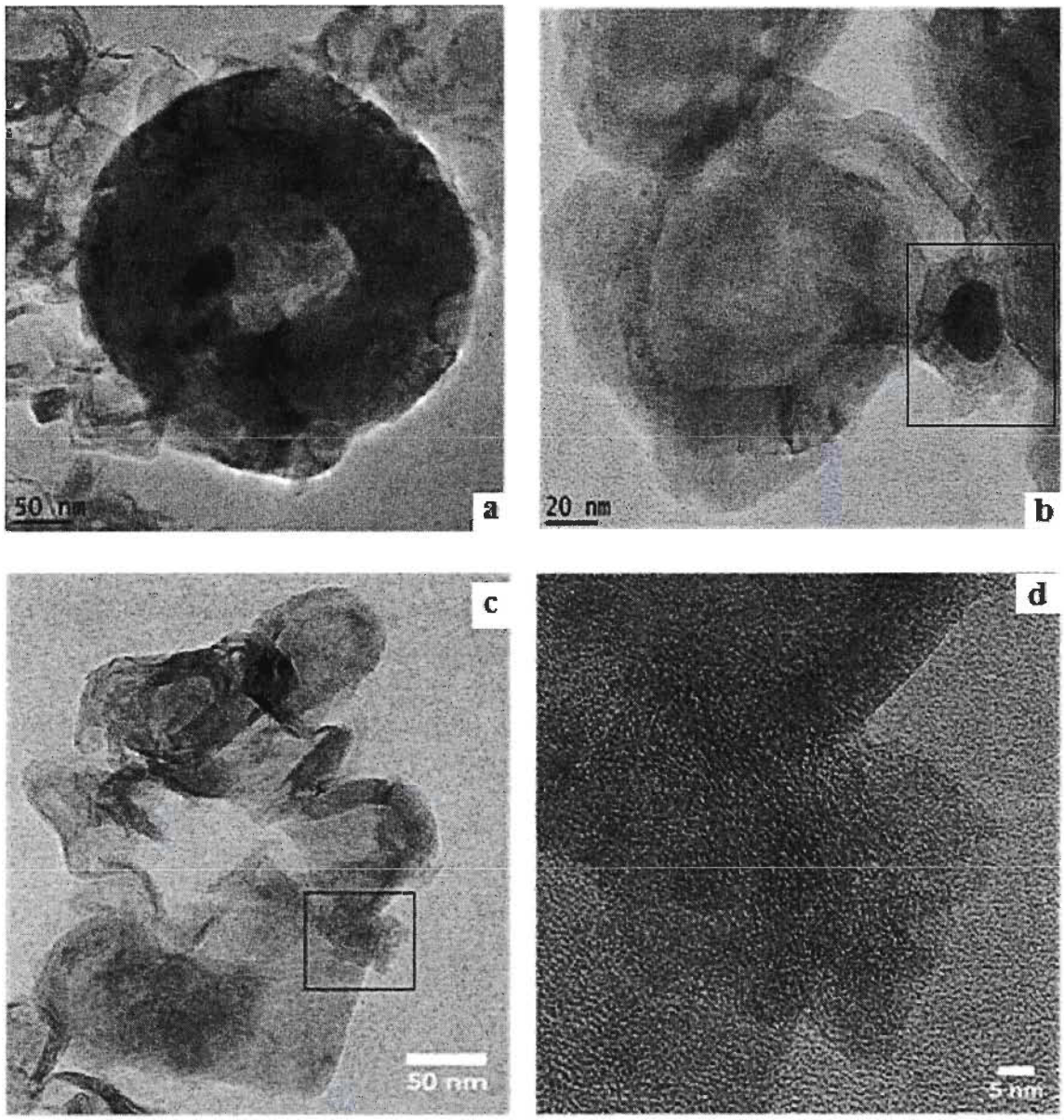

Figure 3.13 : (a) Image TEM d'un ruban nanographitique unique ayant la forme d'une beigne. (b) Nanoparticule de fer entourée de plans graphitiques. (c) Rubans nanographitiques et carbone amorphe. (d) Agrandissement de la portion d'image dans le rectangle de l'image (c).

La Figure 3.14 présente les spectres Raman du CNS201 et des échantillons SPEX et planétaire broyés. On y observe la bande D et G dont les valeurs sont listées aux Tableau 3.1. La longueur moyenne des plans graphitiques du noir de charbon est L_a = 2 mm.

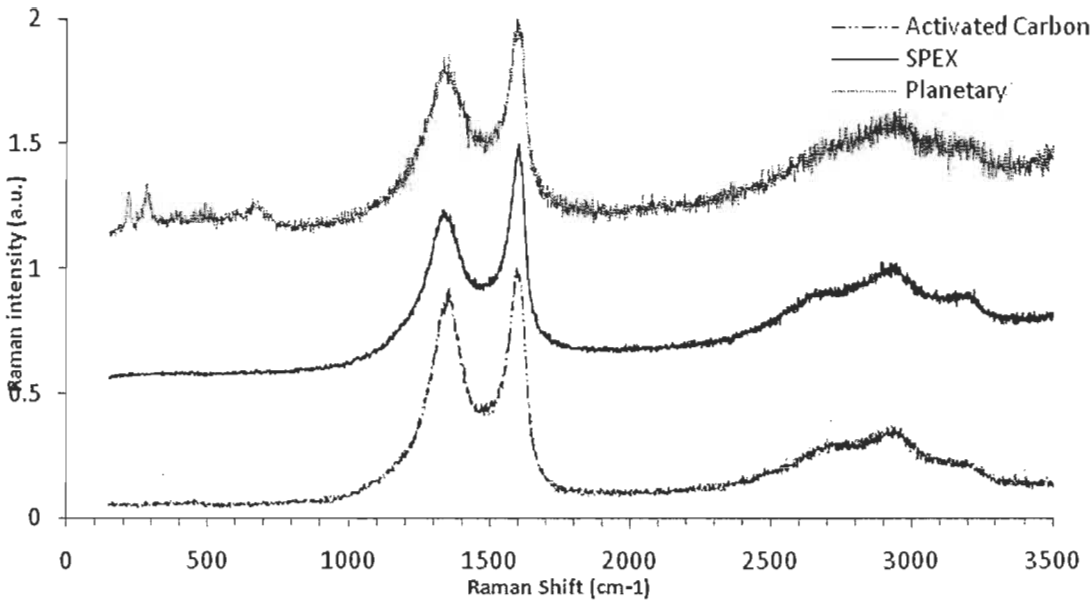

Figure 3.14 : Spectres Raman du charbon activé CNS201, d'un échantillon SPEX broyé (12 h), et d'un échantillon planétaire broyé (24 h).

La Figure 3.15 présente les spectres Raman des échantillons SPEX et planétaire broyés et chauffés à 700 °C pendant 90 minutes sous argon. On y observe l'apparition de la bande 2D qui est une caractéristique des réseaux graphitiques ordonnés.

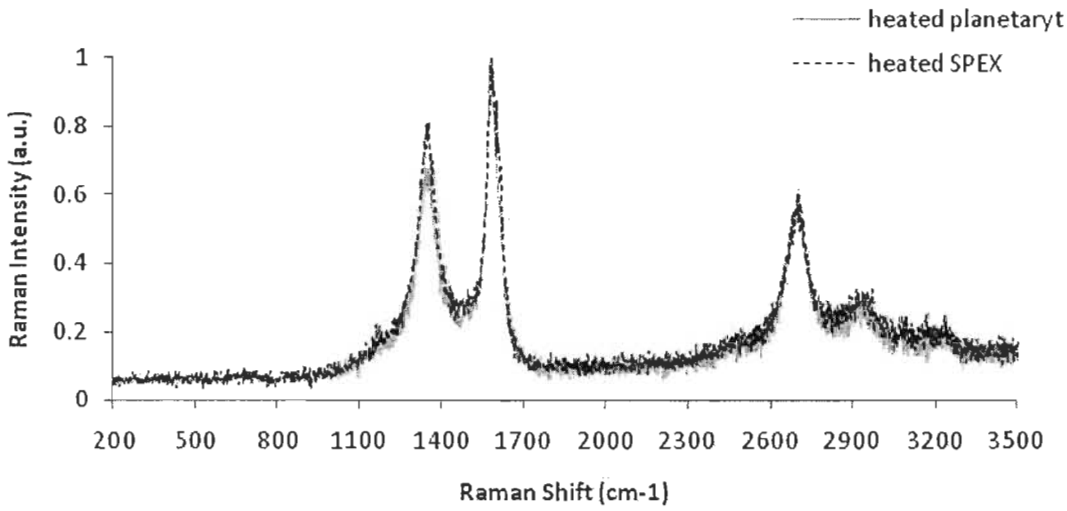

Figure 3.15 : Spectres Raman des échantillons SPEX et planétaire après chauffage à 700 °C pendant 1.5 h.

Finalement, les spectres Raman des échantillons purifiés au HCl sont présentés à la Figure 3.16. Ces spectres montre que les CNS n'ont pas été détruits par le traitement au HCl mais que la quantité de carbone amorphe a diminué parce que la hauteur de la bande 3D, centrée à 1,500 cm^{-1} entre les bandes D et G, a diminuée. Le Tableau 3.1 liste les valeurs des positions des bandes D, G et 2D des échantillons après broyage, après chauffage et après purification. La position à haut énergie de la band 2D ≈ 2700 indique un haut degré d'ordre dans l'empilement des plans de graphène formant les cristallites.

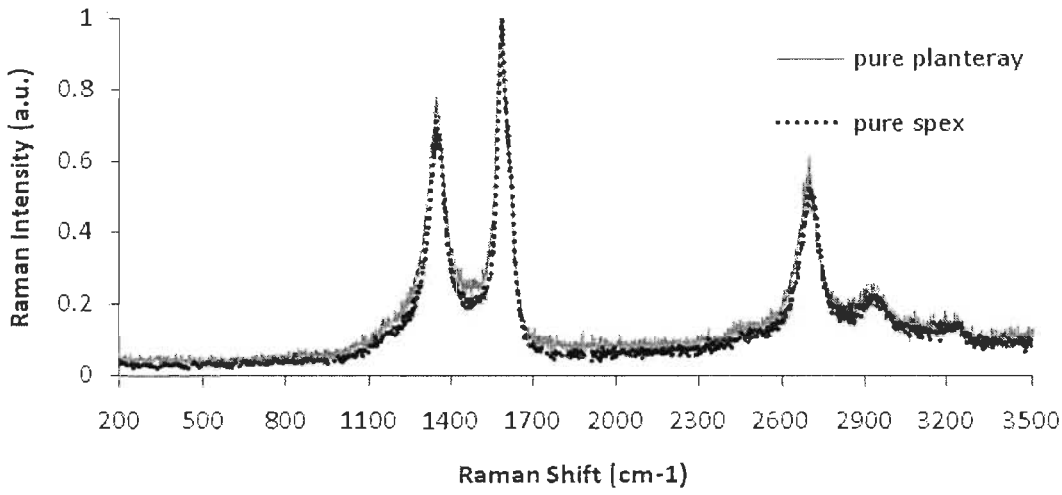

Figure 3.16 : Spectres Raman des échantillons SPEX et planétaire après purification au HCl pendant 3 h.

Tableau 3.1 : Positions des bandes D, G, et 2D des spectres Raman des échantillons SPEX et planétaire.

	Échantillon	Position de la bande Raman (cm^{-1}) [1]		
		bande-D	bande-G	bande-2D
Matériel de base	Charbon activé	1,360	1,595	-
Après broyage	SPEX	1,333	1,601	-
	planétaire	1,355	1,596	-
Après chauffage	SPEX	1,352	1,580	2,702
	planétaire	1,350	1,582	2,697
Après purification	SPEX	1,343	1,582	2,702
	planétaire	1,344	1,577	2,696

La Figure 3.17 faite par Larouche et Stanfield [25] présente une nouvelle classification proposé par ces auteurs pour différents carbones structurés et incluant nos CNS. Cette classification porte en graphique la longueur équivalente moyenne L_{eq} des plans graphitiques courbés avec

$$L_{eq} = 8.8 \left(\frac{A_{2D}}{A_D}\right),$$

où A_D et A_{2D} sont les aires des bandes D et 2D, respectivement, en fonction de la largeur de la bande 2D à mi-hauteur $\Delta\omega_{2D}^{-1}$. La Figure 3.17 montre que nos CNS possèdent un plus haut degré de graphitisation comparé à la plus part des autres échantillons.

[1] La précision instrumentale de cette mesure est ± 1 cm^{-1}.

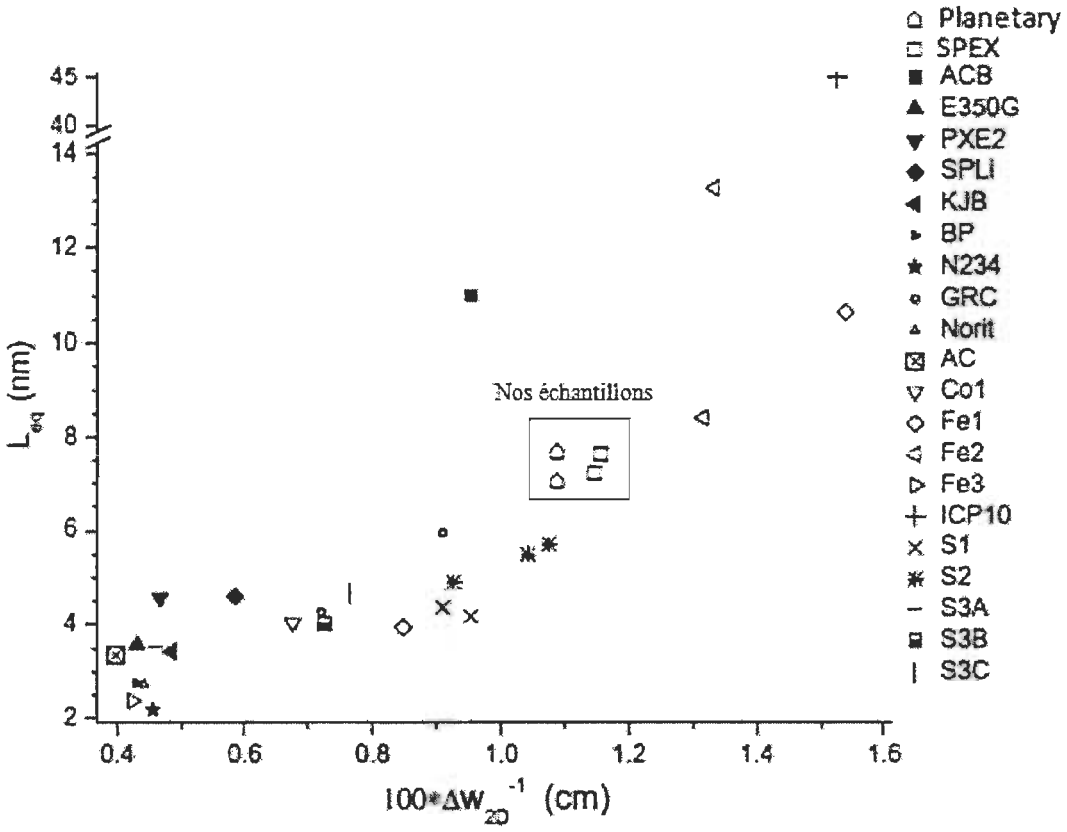

Figure 3.17 : Classification de charbons nanostructurés utilisant L_{eq} en fonction de $\Delta\omega_{2D}^{-1}$ de la référence [25] incluant des échantillons SPEX et planétaire.

Le Tableau 3.2 liste les résultats des mesures d'adsorption d'isothermes de N_2 à 77 K des échantillons SPEX et planétaire purifiés. La surface totale obtenue par analyse BET [27] et la surface externe obtenue par analyse t-Plot [31] sont plus grandes pour l'échantillon planétaire tandis que la surface des micropores pour l'échantillon SPEX est plus que deux fois supérieurs à celle de l'échantillon planétaire. La Figure 3.18 montre les courbes d'adsorption et de désorption des deux échantillons purifiés. Ces courbes sont de type IV et l'hystérèse entre $0.4 < P/P_0 < 0.99$ indique que nos CNS sont principalement mésoporeux.

Tableau 3.2 : Surface spécifique BET, surface externe et surface et volume microporeux des échantillons SPEX et planétaire purifiés.

	Surface spécifique BET (m^2/g)	Surface externe m^2/g (t-Plot)	Surface microporeuse m^2/g (t-Plot)	Volume microporeux cm^3/g (t-Plot)
SPEX	157.3	144.8	12.5	0.007
Planetary	197.3	192	5.3	0.0046

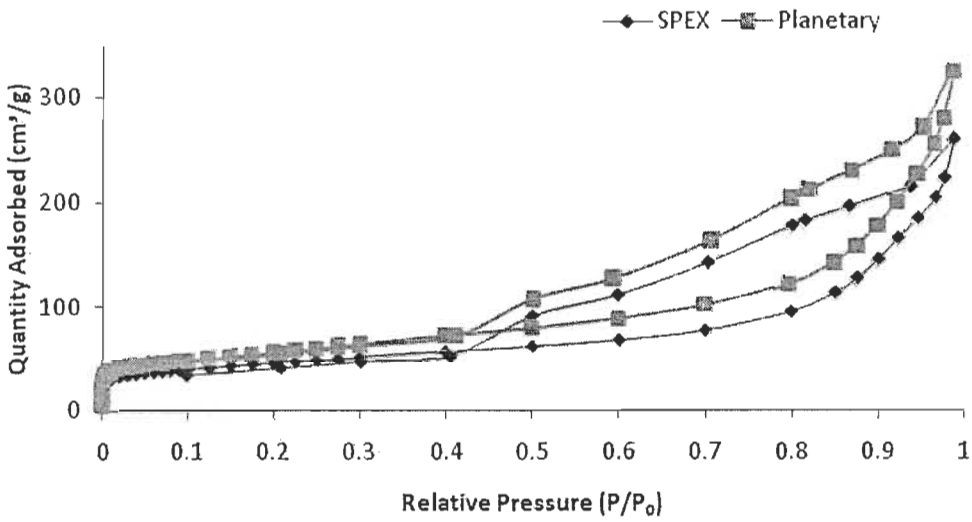

Figure 3.18 : Isothermes d'adsorption et de désorption N_2 des échantillons SPEX et planétaire purifiés.

La Figure 3.19 montre le volume de mésopore cumulatif (en desorption) des deux échantillons en fonction de la dimension des pores qui varie de 3 à 50 nm. L'analyse a été faite par la méthode BJH (Barrett, Joyner, and Halenda) et conclut que l'échantillon planétaire a un volume mésoporeux plus grand que l'échantillon SPEX. La Figure 3.20 montre le volume de mésopore/macropore cumulatif en fonction de la dimension des pores en échelle logarithmique. L'analyse a été faite par la méthode DFT (*Density Functional Theory*) [32] et conclut que l'échantillon planétaire a un volume mésoporeux et macroporeux plus grand que l'échantillon SPEX, en accord avec la méthode BJH.

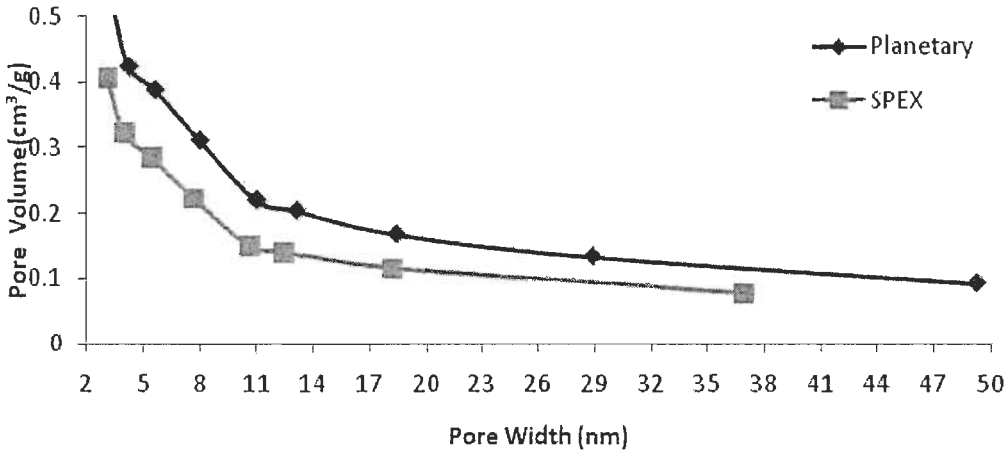

Figure 3.19 : Volume poreux cumulative BJH (désorption) en fonction de la taille des mésopores pour des échantillons SPEX et planétaire purifiés.

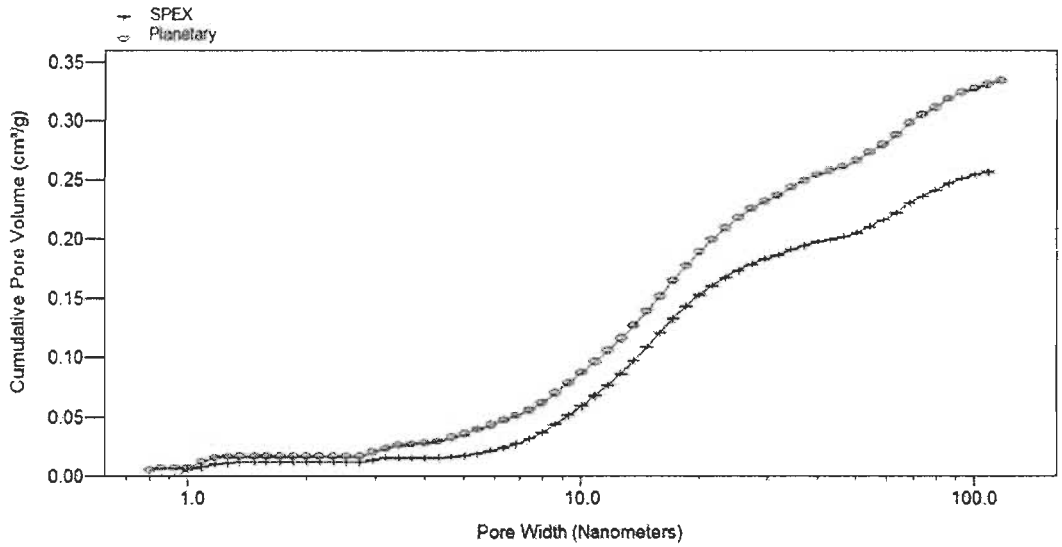

Figure 3.20 : Distribution des volumes poreux cumulatifs DFT en fonction de la taille des méso/macropores pour des échantillons SPEX et planétaire purifiés.

La Figure 3.21 montre les résultats des mesures d'intrusion au mercure pour les deux échantillons purifiés. La courbe du volume de méso/macropores en fonction du rayon des pores pour l'échantillon SPEX a un pic distinct pour un rayon de pore d'environ 1 μm correspondant à un volume poreux de 160 mm^3/g. La courbe pour l'échantillon planétaire a deux pics à environ 0.1 et 1 μm correspondant à un volume poreux de 40 mm^3/g et 80

mm^3/g, respectivement. Pour fin de comparaison, les données pour le Vulcan XC-72 mesurées par Passalacqua *et al.*[28] sont tracées sur la Figure 3.21. Si on compare les pics de nos CNS à 1 μm avec le pic du Vulcan XC-72 à 5.5 μm, ce déplacement du rayon de pore signifie que nos CNS ont un plus grand volume de pore que celui-ci. Ce plus grand volume de pore est attribué à l'espacement entre les nanostructures de nos échantillons.

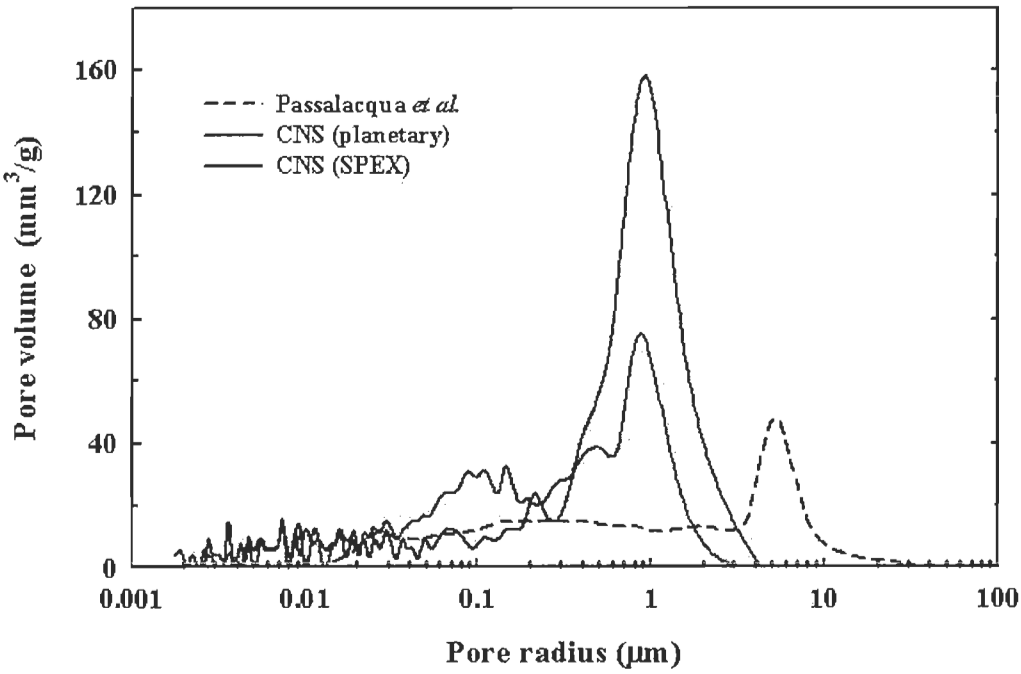

Figure 3.21 : Distribution des volumes macroporeux obtenue des mesures d'intrusion au Hg pour des échantillons SPEX et planétaire purifiés, avec les mesures de la Réf. [28] pour le Vulcan XC-72.

La Figure 3.22 est un graphique de l'analyse thermogravimétrique des échantillons SPEX et planétaire purifiés qui montre une température de décomposition centrée sur 660 °C. Nos échantillons avaient étés préalablement chauffés à 920 °C pendant 1 h sous atmosphère d'argon. Puisque la température d'oxydation de nos échantillons est relativement élevée, nous concluons qu'ils possèdent un degré élevé de graphitisation. De plus, les résultats des TGA font aussi preuve de la pureté des CNS.

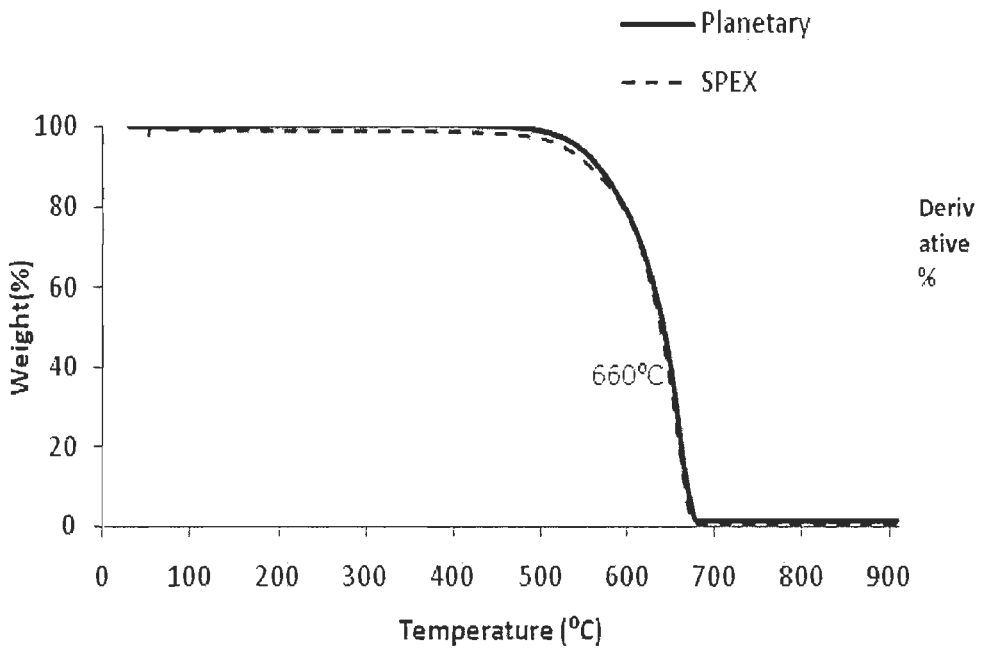

Figure 3.22 : Résultats de l'analyse TGA sous une atmosphère d'air pour des échantillons SPEX et planétaire purifiés.

En conclusion, nous avons présenté une méthode pour produire des carbones nanostructurés avec un haut degré de graphitisation par broyage mécanique d'un charbon activé avec des métaux de transition en présence d'hydrogène. Le broyage est suivi par un chauffage sous atmosphère initial d'argon. Nous avons utilisé deux types de broyeur : des échantillons ont été broyés avec un SPEX (broyage haute énergie) pendant 12 h et des échantillons ont été broyés avec un planétaire (broyage basse énergie) pendant 24 h. Nous avons analysés et comparés les deux types d'échantillons après purification au HCl.

- Les images TEM ont montrées des nanostructures de carbone similaires pour les deux échantillons SPEX et planétaire. Les nanostructures ont la forme de nanoparticules de rubans et de fers à cheval avec des plans graphitiques bien ordonnés mais présentant des défauts. Les deux types d'échantillons contiennent du carbone amorphe et des nanoparticules de fer (27-40 nm de diamètre) entourées de plans graphitiques. L'épaisseur des rubans varie de 5 à 24 nm.
- Les patrons de diffraction aux rayons-X indiquent que les nanostructures des deux types d'échantillons sont essentiellement les mêmes après chauffage et

purification. Les seules différences mineures sont dans les dimensions des cristallites et les espacements entre les plans.

- L'analyse des mesures d'adsorption de N_2 à 77 K a montré que la surface totale de l'échantillon SPEX est 157 m^2/g et 197 m^2/g pour l'échantillon planétaire. Le volume microporeux de l'échantillon SPEX (0.007 cm^3/g) est presque le double de l'échantillon planétaire (0.0046 cm^3/g).
- L'analyse des mesures d'adsorption et de désorption de N_2 à 77 K a montré que les deux types d'échantillons sont principalement méso/macroporeux. L'analyse BJH de désorption et l'analyse DFT ont démontré que le volume méso/macroporeux de l'échantillon planétaire est plus grand que celui de l'échantillon SPEX.
- L'analyse des mesures d'intrusion au Hg a montré une distribution des macropores ayant un pic à 1 μm pour l'échantillon SPEX et deux pics à 0.1 μm et 1 μm pour l'échantillon planétaire.
- Les spectres Raman pour les échantillons chauffés et purifiés SPEX et planétaire sont similaires. Selon la classification proposée à la Réf. [25], nos CNS se comparent très bien avec d'autres carbones ayant des hauts degrés de graphitisation.
- L'analyse TGA indique que les deux types d'échantillons ont la même température d'oxydation centrée à 660 °C et qu'ils sont très pures.

Nous concluons d'après les résultats de cette étude que les CNS produits par broyage mécanique de type SPEX et planétaire, suivie des étapes de chauffage et de purification avec les mêmes conditions, ont des nanostructures presque similaires. La seule différence est que l'échantillon SPEX possède un plus grand volume microporeux. Ces rubans de carbones nanostructurés devraient êtres de bons candidats comme support de catalyseurs pour les PEMFCs parce que leur porosité unique pourrait donner une meilleure distribution uniforme des catalyseurs et permettre une meilleure gestion des réactants et de l'évacuation de l'eau.

Abstract

Synthesis of carbon nanostructures (CNS) as a catalyst support for polymer electrolyte membrane fuel cells (PEMFCs) is presented. After ball milling of activated carbon in the presence of hydrogen and transition metals (Fe, Co), followed by heating at 700 °C initially under argon atmosphere, the samples are purified by acid treatment to remove metals and amorphous carbon. Before heating, two types of milled powders are prepared with either a SPEX shaker mills or a planetary mills. On one side, the powder is milled in a SPEX shaker mill for 12 h with a ball-to-powder weight ratio of 35 (usually each batch contains about 1.5 g of powder). On the other side, the powder is milled in a planetary mill for 24 h with a ball-to-powder weight ratio of 10 (usually each batch contains about 20 g of powder). Characterization of CNS prepared by two different mills after HCl purification is performed. X-ray diffraction patterns (XRD) and Raman spectra of CNS prepared by SPEX and planetary mills indicate similar structures. Transmission electron microscopy (TEM) analysis shows ribbon-like and horseshoe-like CNS with well-ordered graphitic structures. N_2 adsorption and desorption isotherms diagram shows that both CNS samples are mainly meso/macroporous. Thermal gravimetric analysis (TGA) indicates that both SPEX and planetary samples have the same oxidation temperature centered at 660 °C .It was revealed that SPEX sample has higher pore volume and slightly better graphitic structures that makes it a good candidate as a catalyst support for PEMCS.

Acknowledgments

I would like to thank my supervisor Dr. Jean Hamelin for giving me the opportunity to study my master with him. He has been an amazing supervisor and one of the best professors I ever had. I sincerely appreciate his immense support and encouragement during my studies and especially while I was writing this thesis.

I would like to thank Daniel Cossement, Sadesh Kumar Natarajan, Nicholas Larouche, Marie-Eve Marchand, Lyubov Lafi, Marie-Hélène Bégin, Agnes Lejeune, Jean-Philippe Masse and François Morin for their collaboration and technical expertise. I really appreciate Dr. Louis Marchildon, Dr. Jacques Huot, Lucie Bellemare, Hélène Boisclair and my colleagues in the *Institut de recherche sur l'hydrogène* (IRH). Special thanks to my parents for their love and support.

I am so thankful to Hydro-Québec for a two-year scholarship and for the financial support of Natural Sciences and Engineering Research Council of Canada (NSERC) and Physics Department of the *Université du Québec à Trois-Rivières.*

Table of contents

List of figures

List of tables

Introduction

Technology of Polymer Electrolyte Membrane Fuel Cell (PEMFC) has made rapid progress in recent years. Improving the long-term performance of carbon supported catalysts is considered as one of the most important problems to be solved for the marketing of PEMFCs. The central part of a PEMFC is the membrane electrode assembly (MEA), which consists of two electrodes (anode and cathode) and a cation exchange membrane. These electrodes are usually made of carbon black (the Vulcan XC-72) supported on carbon paper or carbon cloth. The catalyst layers (CL) are part of the electrodes where electrochemical reactions take place and are composed of a catalyst (Pt or Pt alloy) supported by carbon black. As mentioned above, the durability of CLS is the crucial problem for the development of PEMFCs.

Despite widespread use, carbon black is subject to electrochemical oxidation by surface oxidation that eventually turns into CO_2 in the cathode where it is subject to high levels of acidity, temperature and humidity. When the carbon is oxidized, the metal catalyst nanoparticules will be lost to the electrode or agglomerate into larger particles. Oxidation of carbon support can also lead to changes in surface hydrophobicity, which can lead to difficulties of transporting gas.

Several research groups have proposed that carbon with higher degree of graphitization can be more resistant to corrosion in the cathode. Furthermore, carbon with larger pore volume and microporosity can be more effective in water transport in/on the cathode layer.

This research project focuses on the fabrication and characterization of carbon nanostructures as a catalyst support for polymer electrolyte membrane fuel cells (PEMFCs). The process of carbon nanostructures (CNS) is ball milling of activated carbon in the presence of transition metals (Fe, Co) and hydrogen at the pressure of 1.4 MPa followed by heating at 700 °C in argon atmosphere. Different types of milling equipments such as SPEX shaker mills (high-energy mills) and planetary mills (low-energy mills) are used to produce mechanically milled powder. After preparation of CNS

in order to remove metallic nanoparticules and amorphous carbon, sonication of CNS in hydrochloric acid for 3 h is performed.

In our work we were facing a major problem. We could not reproduce the CNS that synthesis method was originally developed in the laboratories of the *Institut de recherche sur l'hydrogène* (IRH). Our samples still had a large amount of iron carbide that is not removed by acid treatment and prevents the formation of carbon nanostructures. After several months of research we found that the base metals, iron and cobalt, were contaminated. (The results are presented in Appendices I and II)

For many years, SPEX mills have been used for CNS fabrication in IRH .With SPEX mills just 2 g of CNS can be prepared and before ball milling, the crucible should be evacuated 1 h and introduced to hydrogen overnight. Meanwhile, with planetary mills, the large scale preparation of CNS (20 g) as well as quick evacuation and hydrogen introduction (less than 5 minutes) was observed. Study and analysis of graphitization degree, porosity, microstructure and stability of CNS prepared by SPEX and planetary mills are mainly explained in this project. The principal objectives of the project include:

- Study the synthesis of carbon nanostructures (CNS) by the method developed by Natarajan *et al.* [5].
- Study the behavior of activated carbon with Fe and Co under hydrogen atmosphere during ball milling with SPEX and planetary mills.
- Develop a transition metal purification procedure.
- Study the porosity (size and volume of pores), morphology, microstructure, stability and graphitization degree of pure CNS prepared by SPEX and planetary mills.
- Improve the microspore and macrospore surface area of CNS.

In Chapter 1 we give an overview of fuel cells, catalysts, and catalyst support. Fabrication of carbon nanostructures (synthesis and theory) and characterization techniques are presented in Chapter 2. Results and discussion after characterization of CNS by X-ray diffraction, N_2 adsorption, Hg intrusion, Raman spectroscopy, TEM, and TGA are investigated in Chapter 3. We present a summary of our initial results and

different purification methods used to remove impurities in Appendix I, the source of contamination in our sample is explained in Appendix II and the supplementary results including the increase of micropore surface area are presented in Appendix III.

Chapter 1: Generality

1.1 Fuel cells

A fuel cell is an electrochemical device that converts chemical energy into electrical energy and heat. The most popular fuel cell is the polymer electrolyte membrane fuel cell (PEMFC). The distinguishing features of PEMFCs include relatively low-temperature (under 90°C) of operation, a high power density, a compact system, and ease of handling.

Since PEMFCs can generate power from a watt to hundreds of kilowatts, they can be used in almost all applications, from vehicles to mobile phones. Applications for transportation, such as automobiles and buses have already been demonstrated. Also, fuel cells are attractive as backup power generators compared with internal combustion engine generators (due to noise, reliability, and maintenance considerations). Small PEMFCs as portable power generators have several advantages over conventional batteries and can replace them in the future [1]. The major drawbacks of batteries for these applications are limited capacity and slow recharging, whereas a fuel cell system can achieve higher power and energy capacity. In addition, battery performance deteriorates when the charge drops, whereas fuel cells operate at a constant level as long as fuel is supplied. A schematic representation of a PEM fuel cell is shown in Figure 1.1.

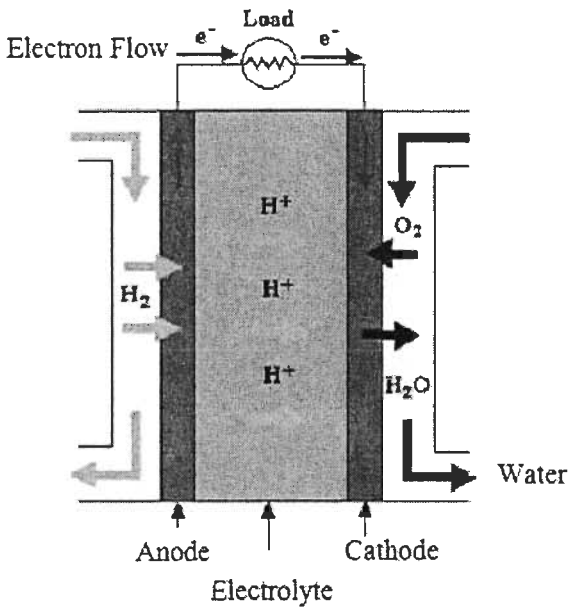

Figure 1.1: Schematic representation of a PEMFC

As seen in Figure 1.1, hydrogen is delivered to the anode side of the cell through the flow field channels. Then, hydrogen is decomposed into positively charged protons and negatively charged electrons. Protons migrate through the membrane towards the cathode, whereas electrons travel along an external circuit and produce an electrical current. On the cathode, the electrons recombine with the protons, and together with the oxygen molecules, form water as the only reaction by-product, which flows out of the cell.

The important part of PEM fuel cells, the membrane electrode assembly (MEA), consists of a polymer electrolyte membrane sandwiched between two electrodes. The main function of the membrane in PEM fuel cells is to transport protons from the anode to the cathode; membrane polymers have sulfonic groups, which facilitate the transport of protons. The other functions include keeping the fuel and oxidant separated, which prevents mixing of the two gases and withstanding harsh conditions, including active catalysts, high temperatures or temperature fluctuations, strong oxidants, and reactive radicals. Thus, the ideal polymer must have excellent proton conductivity, chemical and thermal stability, strength, flexibility, low gas permeability, low water drag, low cost and good availability [1]. One of the most widely used membranes today is Nafion, a polymer created by the DuPont Company.

On the surfaces of the two electrodes, two electrochemical reactions take place. On the anode, hydrogen atoms are oxidized and on the cathode, oxygen is reduced. The two electrode reactions are as follows:

Anode reaction $H_2(g) \rightarrow 2H^+ + 2e^-$

Cathode reaction $1/2O_2 + 2H^+ + 2e^- \rightarrow 2H_2O$

Overall reaction $1/2O_2 + H_2 \rightarrow 2H_2O$

1.2 Catalyst and catalyst support for PEMFC

Catalysts for PEMFCs are typically nano-size range platinum (Pt) supported on carbon black with loadings of about 0.3 mg/cm^2. Pt is the most commonly used catalyst for both cathode and anode in PEMFCs.

On the anode in the case of pure H_2, the reaction kinetic is so fast that low-loading Pt is sufficient hence the cost is not a cause of concern. The presence of a little amount of carbon

monoxide (CO) in the hydrogen gas can strongly adsorb on the Pt catalyst in the anode. The adsorbed CO, even 10 ppm, blocks the catalytically active area, thereby significantly decreasing its reactivity and causing so-called "CO poisoning". Consequently, Pt-Ru alloys may be used in the anode to enhance catalytic activity in the presence of CO. On the cathode, where O_2 is reduced (ORR - Oxygen Reduction Reaction), Pt is the most commonly used catalyst. However, the ORR reduction kinetic is slower, the amounts of Pt and hence the cathode catalyst costs are high. Combination of Pt with metals can be considered to improve catalytic activities and replacing at least some of the Pt. The environment for both anode and cathode reactions of PEMFCs is acidic and that restricts the number of metals that can be used as a catalyst.

Usually, the platinum catalyst is formed into small particles in the single nm-range and dispersed on a surface of larger particles that act as a supporter, which is usually a carbon powder. In this way platinum is highly divided, so that a very high proportion of the surface area will be in contact with the reactant, resulting in a great reduction with an increase in power. At the beginning of PEM fuel cell development, the rate of 28 mg/cm^2 of platinum was loaded for catalyst while, recently, the usage has been reduced to around 0.2 mg/cm^2 with an increase in power [2].

Catalyst stability is a greater concern for the cathode than the anode, as in a fuel cell the cathode operates at very positive potentials, enhancing corrosion of the catalyst and catalyst support. Corrosion of carbon as Pt-support results in missing or aggregation of catalyst nanoparticules that deteriorate fuel cell performance. For example, a cathode catalyst comprising 40% Pt on a Vulcan XC72R carbon support showed a rate of carbon loss at 1.42 V of 1650 mg/day. It has been reported that more graphitic carbon structure is more stable and resistant to corrosion [3].

Water management in the cathode has a great importance. Water formation due to oxygen reduction reaction (ORR) can fill pores of catalyst and catalyst support and make them inactive. Water gradually accumulates in the larger hydrophilic pores and hence flooding the electrode. In smaller hydrophobic pores there is no blockage and droplet might grow on pore wall. The smallest hydrophobic pores are less prone to flooding [4].

1.3 Carbon nanostructures as a catalyst support for PEMFCs

Natarajan *et al.* [5] investigated the fabrication of a new type of carbon nanostructures (CNS). The process consists in two stages: 1) Ball milling of activated carbon in the presence of H_2 and transition metals (Fe, Co) for 12 h. 2) Heating of the milled sample at 700 °C for 90 minutes under an initially inert atmosphere and subsequent formation of CNS on the metallic nanocrystals. Characterization and analysis of these CNS have demonstrated a higher degree of graphitization and higher surface area with a larger pore volume in comparison with carbon black. Next, Natarajan *et al.* [6] developed a purification and functionalization method and followed by platinization resulting in a homogeneous distribution of the catalyst on the CNS surface. Subsequently, Natarajan *et al.* [7] performed electrochemical durability tests of Pt supported on CNS (Pt/CNS) and compared them with Pt supported on Vulcan XC-72 (Pt/C).

1.4 Carbon nanostructures

There are many methods to produce CNS like arc-discharge, laser ablation and chemical vapor deposition (CVD) [8]. The most widely used method is CVD, which has certain advantages such as high yield, low cost, controllable growth conditions and more defect formation in the CNS. However, the CNS produced by CVD technique are usually long, tangled together and have closed ends [9]. In this study, we use ball milling of activated carbon in the presence of iron and cobalt under hydrogen atmosphere and subsequent annealing in argon atmosphere. This simple method is similar to CVD where carbon nanostructures are formed on metallic nanoparticules. Marshall and Wilson [10] studied the ball milling and heating of graphite in the presence of cobalt (1 wt.% and 10 wt.%). They found out that ball milling of graphite with 1 wt.% cobalt introduces some defects into the graphite structure and upon subsequent annealing, the graphite becomes ordered. However, under the same ball milling conditions of graphite with 10 wt.% cobalt, graphite reaches a higher degree of structural order than those with 1 wt.% cobalt (This process is attributed to the pinning effect of cobalt during ball milling) as well as during annealing the sample containing 10 wt.% cobalt, the carbon is reorganized more effectively than in the sample with 1 wt.% cobalt.

Bokhonov and Korchagin [11] investigated morphological and structural changes during high energy ball milling and heating of soot-iron and soot-nickel. It was shown that during ball milling of soot-iron, the formation of cementite Fe_3C phase occurs and the decomposition of iron carbide during heating leads to the formation of a crystalline carbon phase. The same process happens to soot-nickel. They observed that for the soot–iron system, the temperature at which the amorphous carbon starts to crystallize is 250-300 °C while for the soot-nickel this temperature is 600 °C.

After the preparation of CNS, effective purification is needed to remove all by-products of synthesis process, as undesired carbonaceous phases (amorphous carbon and nanoparticules) and catalyst particles. Several purification techniques, both physical and chemical, have been used depending on morphology, growth process and metal catalyst [12]. It is well-known that chemical methods such as acid oxidation, gas oxidation, nitric acid reflux, mixed nitric/sulphuric acid reflux, result in higher purity CNS but introduce also chemical defects into the CNS structure. Fogden *et al.* [13] found out that acid treatments also produce molecular debris that can remain adsorbed onto the CNS, even after conventional water washing. They propose to add dilute base-washing step to obtain higher purity sample. This treatment converts the weaker acidic groups to their conjugate salts, increasing the solubility of the impurities in water. Subsequent treatment with dilute acid can be used for further functionalization.

Our purification method was based on the sonication of CNS powder suspended in 6 M HCl and placed in an ultrasonic bath for 3 h. In the ultrasonic bath, the sound waves radiate through the solution in the tank, causing high and low pressures. During the low pressure stage, millions of microscopic bubbles form and grow. During the high pressure stage the bubbles collapse releasing an enormous amount of energy. These implosions act like an army of tiny scrub brushes. They work in all directions, attacking every surface and invading all recesses and openings.

Chapter 2: Experimental

2.1 CNS synthesis

We start with high surface area activated carbon (99.9% pure), pre-heated at 1,000 °C in vacuum for 1 h in order to remove adsorbed nitrogen, oxygen and water vapour. In a hardened steel crucible, 50 wt.% of activated carbon is mixed with 44 wt.% of Fe (Aldrich, 93% pure < 212 μm) and 6 wt.% of Co (Aldrich, 99.9% pure < 150 μm). All the manipulations are done in a glove box under argon atmosphere. The crucible was evacuated for 1h, then hydrogen at the pressure of 1.4 MPa (200 psig) is introduced into the crucible overnight. Ball milling is carried out at room temperature in SPEX® shaker mills for 12 h with 1.5 g powder and three to six hardened steel balls with ball-to-powder weight ratio of 35. Ball milling was also done in planetary mills, Fritsch Pulverisette 5, with steel container and balls for 24 h. The speed of main disk was 300 rpm. The starting material, their proportion and hydrogen pressure are the same as SPEX mills. Since planetary mills have lower energy, time of milling and number of balls are different from those of SPEX. For planetary mills, 20 g of powder was milled with thirty steel balls with a ball-to-powder ratio of 10. The next stage was heating the milled powder in a quartz tube to 700 °C for 90 minutes under an initial argon atmosphere.

Purification of CNS was as follows: 400 mg of powder was suspended in 200 ml of 6 M HCl (36%) and sonicated in an ultrasonic bath (Cole-Parmer model 8891) for 3 h at 40 °C. After sonication, the sample was filtered through an 8μm filter paper and washed with demonized water and dried in air at 200 °C.

2.2.1 Type of mills

SPEX and planetary mills are two different milling tools to produce mechanically alloyed powder. SPEX shaker mill has one vial, containing the powder sample and balls, protected by a clamp and swung energetically back and forth several thousand times a minute. The back-and-forth shaking motion is combined with lateral movements of the ends of the vial, so that the vial appears to be describing a figure 8 or infinity sign as it moves. With each swing of the vial the balls impact against the sample and the end of the vial, both milling and mixing the sample. Because of the amplitude (about 5 cm) and speed (about 1,200 rpm) of

the clamp motion, the ball velocities are high (about 5 m/s) and consequently the force of the ball impact is unusually great. Therefore, these mills can be considered as high-energy variety.

Planetary ball mill: the planetary ball mill is one of the most popular mills; it owes its name to the planet-like movement of the vials. It consists of vials and rotating support disk, rotating around their own axes. The centrifugal force produced by the vials rotating around their own axes and produced by the rotating support disk both act on the vial contents, consisting of powder sample and balls. Since the vials and the supporting disk rotate in opposite directions, the centrifugal forces alternatively act in one direction and the opposite one. The balls in the planetary mills acquire much higher impact energy than it is possible with simple gravity or centrifugal mills. The impact energy depends on the speed of the planetary mill; it can reach about 20 times more than the earth acceleration. Planetary ball mill in comparison with SPEX produces lower mechanical energy [14, 15].

2.2 Theory

Generally, ball milling of carbon and transition metal causes a breakdown of the carbon bonds, dispersion of metal particles to nanometer sizes, formation of metal-carbon and carbide-carbon aggregates [10]. During ball milling in hydrogen, the broken carbon bonds are saturated with hydrogen and may produce methane gas (CH_4). Ball milling in hydrogen also can prevent agglomeration [16]. The chemistry of methanation can be described with the following reaction:

$$FeC + 4FeH \rightarrow CH_4 + 5Fe,$$

which involves the following sequence of elementary steps:

1. The following reaction involves the reversible dissociative adsorption of hydrogen on the iron surface,

$$H_2 + 2Fe \leftrightarrow 2Fe\text{-}H_{ads}.$$

2. During the mechanical synthesis, the carbon gets adsorbed on the metallic iron surface,

$$Fe + C \rightarrow Fe\text{-}C_{ads},$$

which is hydrogenated by the adsorbed atomic hydrogen in the following steps,

$$FeC + Fe\text{-}H_{ads} \rightarrow Fe\text{-}CH_{ads} + Fe,$$

$$Fe\text{-}CH_{ads} + Fe\text{-}H_{ads} \rightarrow Fe\text{-}CH_{2ads} + Fe,$$

$$Fe\text{-}CH_{2\,ads} + Fe\text{-}H_{ads} \rightarrow Fe\text{-}CH_{3ads} + Fe,$$

$$Fe\text{-}CH_{3\,ads} + Fe\text{-}H_{ads} \rightarrow CH_4 + 2Fe.$$

During the heating process, the following reactions are assumed: first, desorption of hydrogen and hydrocarbon formation over the transition metals at 300 °C, then catalytic decomposition of hydrocarbons over the transition metals and formation of carbon nanostructures along with hydrogen production over 600 °C [5]. Decomposition of one mole of methane in the absence of oxygen produces two moles of hydrogen and carbon nanostructures. Thermal energy requirement to produce one mole of H_2 is 37.8 kJ/mol,

$$CH_4 \rightarrow C_{CNS} + 2H_2 . \qquad (\Delta H^{\circ} = +75.6 \text{ kJ/mol})$$

2.3. Characterization techniques

A number of techniques are commonly used to characterize CNS, including X-ray diffraction patterns for structural analysis, TEM images for microstructural analysis, N_2 adsorption isotherm and Hg intrusion to measure surface area and porosity, TGA to determine thermal stability and Raman scattering.

2.3.1 X-ray diffraction

X-ray diffraction (XRD) is a technique to determine crystal structure, chemical composition and physical properties of materials. XRD is based on observing the scattered intensity of an X-ray beam hitting a sample as a function of the incident angle.

The crystalline structure of heated and purified powder samples were investigated using a Bruker D8 FOCUS X-ray diffractometer. An X-ray tube was used at a power of 40 mA and 40 kV with $CuK_{\alpha 1}$ (λ=1.540600 Å) as radiation source. Samples were mounted in a plastic sample holder. XRD patterns were measured for 2θ values from 10° to 90° at interval of 0.03°. Step times of 1 s per interval were considered. To analyze peaks and determine elements, EVA program was used.

The most common characterization measurement carried out with XRD patterns is the determination of lattice spacing between the graphene layers d_{002}, using Bragg's law:

$$d_{002} = \frac{\lambda}{2 \sin \theta},$$

where λ is the X-ray wavelength of $CuK_{\alpha 1}$ radiation, 1.540600 Å and θ is the position of the 002 diffraction line. Usually, the crystallite size is determined by measuring the Bragg peak width at half the maximum intensity and using the Scherrer formula:

$$L_c = \frac{0.9 \lambda}{B \cos \theta},$$

where L_c is the crystallite size in c-direction (002) and B is the peak width at half the maximum intensity (FWHM). This method can give correct values only if proper corrections to instrumental and strain broadening have been made [14].

2.3.2 Transmission electron microscopy

Transmission electron microscopy (TEM) is a technique for characterizing carbon nanostructures as it provides information on the homogeneity of the sample, on the morphology of the nanostructures, on their microstructure and on the presence of carbon graphite or metal impurities. In TEM images, Bright field is commonly used to view the microstructure of carbon. The larger accelerating the voltage of the TEM, the larger the resolution of the instrument is. Typically, 100 to 400 kV are used to visualize carbon microstructure. Our TEM images were taken at the *École Polytechnique de Montréal* with a JEOL 2100-F microscope. The magnification and the electron energy are 200,000× and 200 kV, respectively. We used TEM images to observe and compare microstructure of purified sample previously milled by SPEX and planetary mills and heated under an argon

atmosphere. TEM images show ribbon-like carbon particles (closed and opened), amorphous carbon and iron nanoparticules. Image J program was used to measure the thickness of the ribbons, the diameter of carbon, metal particle sizes and interplanar distance d_{002}.

2.3.3 Raman spectroscopy

Raman spectroscopy investigates the lattice vibrations of ordered carbon materials as it is extremely sensitive to the graphitic structures. While XRD only provides information on the structure of crystalline materials, Raman spectroscopy can also be used for molecular structures, *i.e.* structures with short-range order. Thus, Raman spectroscopy is widely employed for the characterization of carbon samples, and in particular for carbon nanomaterials like carbon nanostructures. It is well known that the Raman spectrum of carbon nanomaterials presents two first-order bands at frequencies less than 1,700 cm^{-1} region: D band at 1,350 cm^{-1} and G band at 1,580 cm^{-1}. The G band corresponds to the in-plane Raman vibration mode of graphite and is characteristic of the ideal graphitic lattice vibration mode, while the D band is attributed to lattice defects [17, 18].The first overtone of the D band (2D band) is found at 2,710 cm^{-1}. Unlike the D band, the 2D band follows the general selection rule. Therefore, it is always present and its intensity tends to increase with graphitization [17]. In a crystal, the D band is normally prohibited whereas the 2D band is allowed. When the number of defects decreases the 2D band is favored [17-19].

We used Raman spectroscopy to compare Raman spectra from samples after milling, heating and purification. Raman spectroscopy was performed on dried samples at room temperature using a confocal micro-Raman inVia Reflex instrument from Renisthaw with a 514.5 nm Ar laser and a 50× objective mounted on a LEICA optical microscope located in the *Université de Montréal*. The power of laser used is around 300 μW with a focal spot diameter of 3 μm, giving a power of 4×10^7 W/m^2 (this power density is chosen in order to avoid any damage to the samples). The measurement was taken for 75 s and repeated tree times for each sample in the range of 150 to 3,500 cm^{-1}.The calibration is initially made using an internal silicon reference at 520 cm^{-1} that gives a peak position resolution about 1 cm^{-1}.

2.3.4 Nitrogen adsorption isotherm

Nitrogen adsorption isotherm analyses at liquid nitrogen temperature (77 K) were performed using a quantachrome AS-1-MP device to obtain the BET specific surface area and information concerning porosity of CNS powders after purification. Prior to each measurement, samples were outgased at 300 °C under vacuum for 24 h to remove moisture and hydrocarbons vapor and the mass was determined before and after degassing. Data was analyzed by ASAP2020 program.

BET theory is an extension of Langumir theory to multilayer adsorption. If we suppose that gas molecules physically adsorb on a solid in layers infinitely and there is no interaction between each adsorption layer. BET method is expressed by:

$$\frac{1}{\mathrm{V}}\left(\frac{{}^{P}/_{P_0}}{1-{}^{P}/_{P_0}}\right)=\frac{1}{V_m C}+{}^{P}/_{P_0}\left(\frac{C-1}{V_m C}\right),$$

where V is the volume of gas adsorbed and V_{m} is the volume of gas adsorbed at monolayer. P and P_0 are the equilibrium and saturation pressure, C is the BET constant and equal to $C = e^{\frac{E_1-E_l}{k_B T}}$ where E_1 is the heat of adsorption for the first layer of nitrogen, and E_l is for the second and higher layers, k_{B} is Bolzmann constant and T is temperature. A plot of $\frac{1}{\mathrm{V}}\left(\frac{{}^{P}/_{P_0}}{1-{}^{P}/_{P_0}}\right)$ versus ${}^{P}/_{P_0}$ gives a straight line named BET plot. The value of the slope and the y-intercept of the straight line are used to calculate the monolayer adsorbed gas quantity V_{m} and the BET constant C. The linear relationship of BET equation is valid between $0.05 < {}^{P}/_{P_0} < 0.35$. BET specific surface area (m^2/g) can be calculated by multiplying area occupied by one molecule of nitrogen (A_{m} = 0.162 nm^2/molecules), V_{m} (mol/gr) and Avogadro's number N_{A} (molecules/mol):

$$S_{\mathrm{BET}} = V_{\mathrm{m}} \times A_{\mathrm{m}} \times N_{\mathrm{A}}.$$

2.3.5 Thermal gravimetric analysis (TGA)

Thermal gravimetric analysis (TGA) is a technique to estimate corrosion kinetics in high temperature oxidation and determine thermal stability of materials. TGA by raising the temperature gradually, measures the weight loss of sample according to the temperature. A derivative weight loss curve can be used to determine the point at which, weight loss is the highest.TGA analysis was carried out under air atmosphere using a TGA 7 Perkin Elmer apparatus at a rate of 4 °C/min from room temperature to 900 °C.

Chapter 3: Results and discussion

This chapter presents the structural and morphological changes of CNS, prepared by SPEX and planetary ball mills and after heating. The initial samples composition consists of activated carbon 50 wt.%, iron 44 wt.%, and cobalt 6 wt.%.

3.1 XRD analysis of SPEX and planetary mills

Figure 3.1 shows the XRD pattern of the activated carbon (CNS201) used as a raw material to make CNS that was first heated at high temperature (1,000 °C) for 1 h. The heated activated carbon has two broad peaks in the range of $2\theta = 20°$-$30°$ and $2\theta = 37°$-$50°$. According to Sergiienko *et al.* [20], the first broad peak centered at $2\theta = 25.84°$ ($d_{200} = 3.44$Å) is from the short ordered turbostratic carbon. The second broad peak arises from the presence of crystalline iron carbides (Fe_3C) and amorphous iron carbides in cores of carbon nanocapsules. After ball milling the activated carbon, the iron, and the cobalt for 12 and 24 h in SPEX and planetary mills respectively, the crucibles were opened in a glove box (under argon atmosphere) to prevent oxidation. Basically, milling forms fine metal particles, amorphous carbon and iron carbides. Approximately 10mg of the sample was exposed to air while it was put in a sample holder and installed in the XRD diffractometer. As soon as the planetary milled sample was exposed to air, we observed red particles caused by the rapid oxidation of the sample small metal particles. The XRD pattern of the first planetary milled sample showed iron oxide (Fe_3O_4) peaks. Subsequently, we made another sample and we were careful to avoid exposure to air during XRD measurement. In the XRD patterns of the ball milled SPEX and planetary samples of Figure 3.2, we observed two peaks for each sample. For the SPEX milled sample, the XRD pattern was done in air because it did not show any sign of oxidation during manipulation. Its first peak at $2\theta = 31°$ corresponds to short ordered turbostratic carbon but is shifted because of the presence of iron oxide. The iron oxide will be later removed by acid purification. For the planetary milled sample, the first peak that corresponds to short ordered turbostratic carbon is still at $2\theta = 20°$. For both samples, the second peak at $2\theta = 45°$ corresponds to iron and iron carbide. The peaks

corresponding to iron and cobalt do not show because these metals are essentially in an amorphous state.

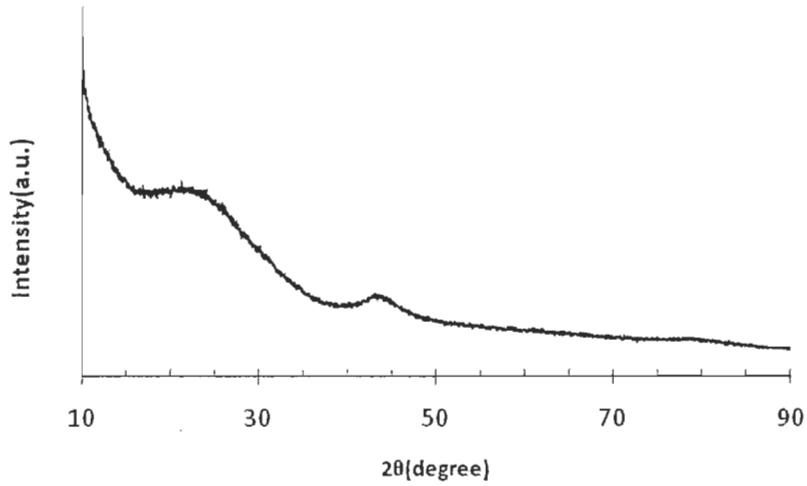

Figure 3.1: XRD diffraction patterns of activated carbon (CNS201).

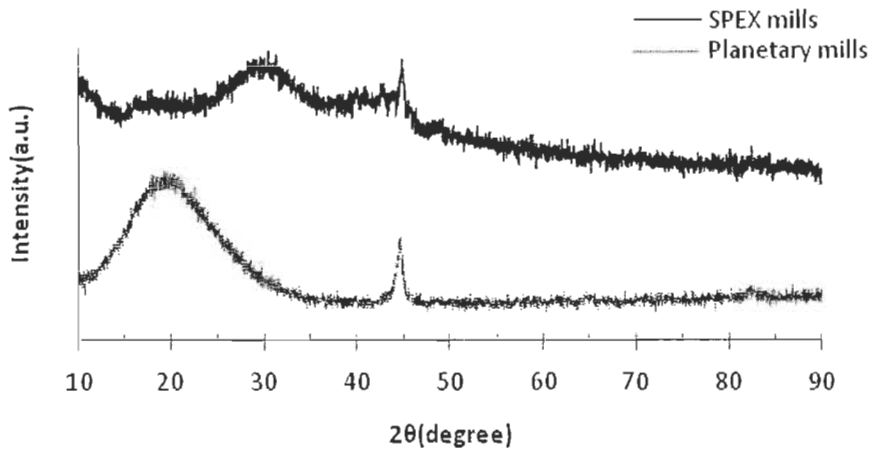

Figure 3.2: XRD patterns of samples after milling in SPEX mills for 12 h and planetary mills for 24 h.

Figure 3.3 shows the XRD patterns of the SPEX and planetary milled samples after heating at 700 °C for 1.5 h under argon. The heating process results in the formation of broad crystalline graphite peak (002) at $2\theta \approx 26.5^{\circ}$ and sharp Fe/Co peaks at $2\theta \approx 44.7^{\circ}$, 65.0° and 82.3°.

The next step is the purification of the heated samples in order to remove metal nanoparticules and amorphous carbon. The purification was done by sonication of the samples suspended in a solution of HCl (6 M) for 3 h. The XRD patterns of Figure 3.4 shows after purification a sharper crystalline graphite peak at $2\theta \approx 26.37^{\circ}$ ($d_{002} = 3.37$ Å) and $2\theta \approx 26.25^{\circ}$ ($d_{002} = 3.39$ Å) for the SPEX and planetary samples, respectively. Smaller peaks associated to Fe/Co are still visible. The crystallite size calculated using Scherrer formula gives 95 Å for the SPEX sample and 82.1 Å for the planetary sample. The bigger crystallite size and smaller d_{002} spacing of the SPEX sample means that the sample has a higher degree of graphitization than the planetary sample [20].

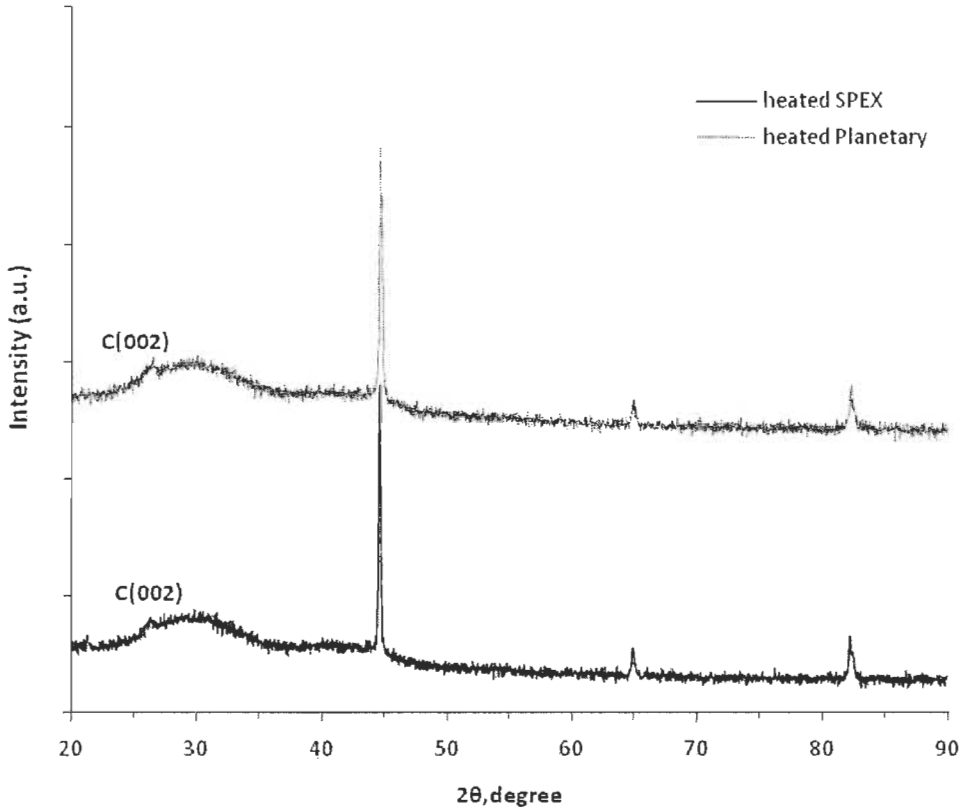

Figure 3.3: X-ray powder diffraction patterns after heating of milled SPEX and planetary samples.

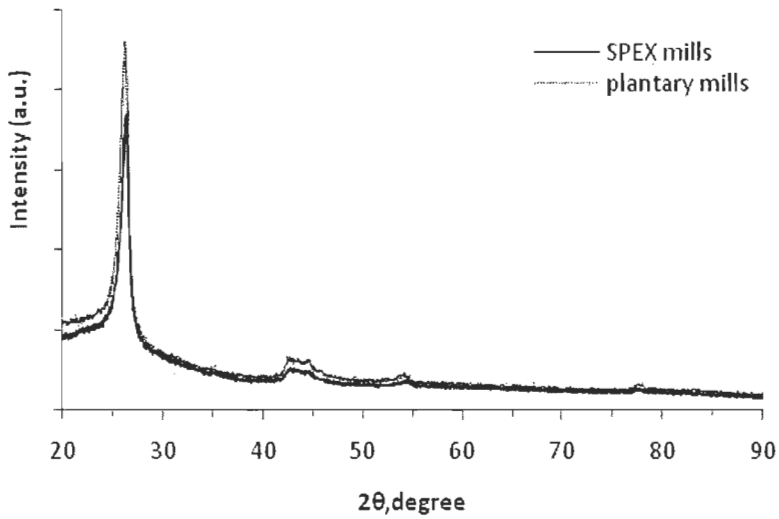

Figure 3.4: XRD patterns of the SPEX and planetary heated samples after purification in HCl for 3 h.

3.2 TEM characterization

3.2.1 Planetary milled sample

Figure 3.5 is a TEM image of a purified planetary sample (milled and heated). The image shows ribbon-like carbon nanostructures with curved diameter ranging from 30 to 220 nm. Some metal nanoparticules (of about 36 nm in diameter) are also visible.

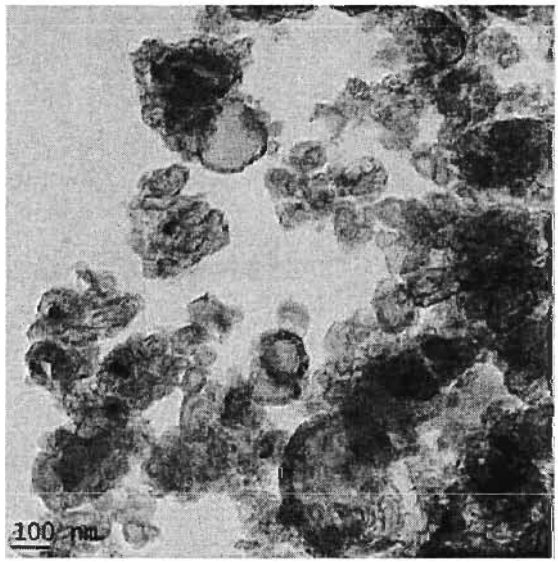

Figure 3.5: TEM image of a purified planetary sample (milled for 24 h and heated at 700 °C for 90 minutes).

From the TEM image of Figure 3.6(a) we can again see the formation of ribbon-like nano structures (nanographite ribbons). In Figure 3.6(a), the thicknesses of the nanographite ribbons are ranging from 8 to 24 nm. It is difficult to measure the length of ribbons since they are entangled with each other. Figure 3.6(b) is the magnification of the image in the rectangle of Figure 3.6(a), where it can be seen that the nanographite ribbon is formed of parallel well-ordered stacked graphitic layers. The thickness of the nanographite ribbon in this image is about 14nm and the distance between graphitic layers (d_{200}) under magnification is estimated to be less than 1 nm.

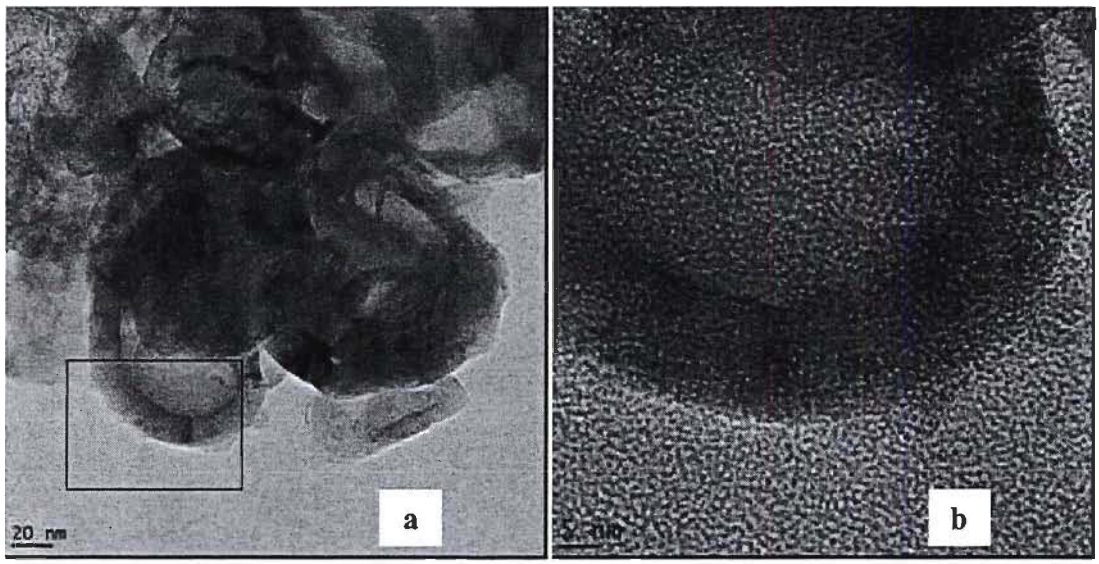

Figure 3.6: (a) TEM images of a purified planetary sample (milled for 24 h and heated for 1 h at 700 °C). (b) Magnification of the image portion in the box of (a).

Figure 3.7(a) is another TEM image showing nanographite ribbon. Figure 3.7(b) is the magnification of the image in the rectangle of Figure 3.7(a), where the thickness of the ribbon is about 12 nm and the distance between graphitic layers (d_{200}) is like in Figure 3.6. It can also be seen in Figure 3.7(b) some defects in the graphitic layers along with well-ordered parts (in the circles). Such defects indicate that the nanographite ribbons have a turbostratic carbon structure. Turbostratic carbon refers to d_{002} spacing ranging from 3.38 Å to 3.44 Å and smaller crystallite sizes (6-20 nm) [21, 22].

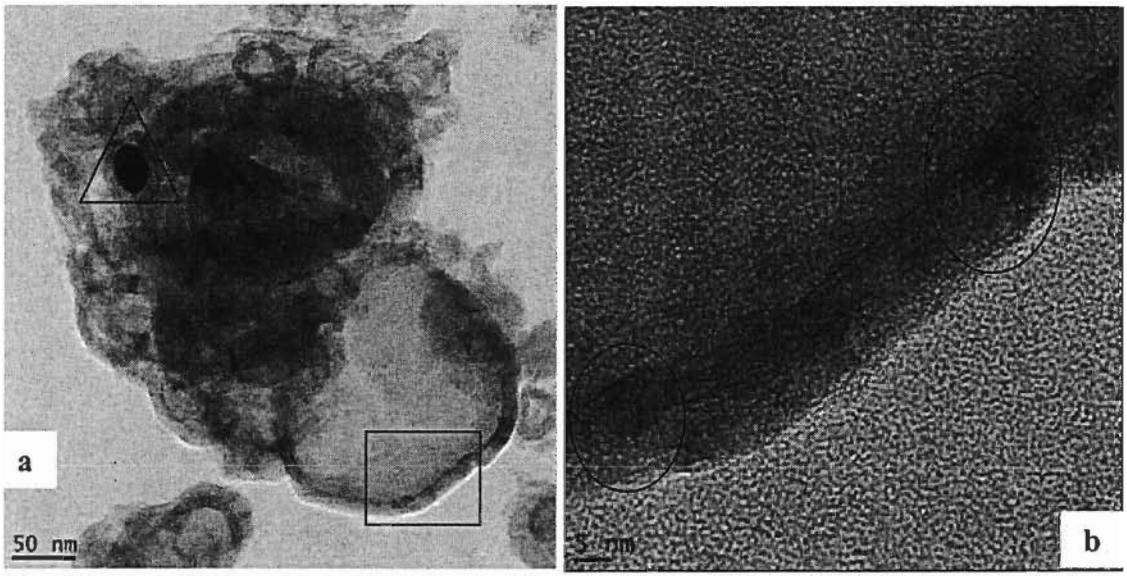

Figure 3.7: (a) TEM images of a purified planetary sample (milled for 24 h and heated for 1 h at 700 °C). (b) Magnification of the image portion in the box of (a).

Figure 3.8(a) is the magnification of the image in the triangle of Figure 3.7(a), where iron nanoparticules are surrounded by graphite layers. The iron nanoparticules are about 40nm in diameter. The thickness of the graphite layers around it is not equal and constant; it differs from 4.5 to 11 nm. In Figure 3.8(b), from another TEM image of the same sample, the iron nanoparticules are 28 nm in diameter and they are surrounded by graphite shells with thickness of 5-7 nm. We mentioned earlier that during annealing, highly ordered graphite carbon structures are forming around iron nanoparticules. During acid treatment, carbon layers start to exfoliate from the surface of iron nanoparticules and form ribbons. Actually, we have observed that thicker nanographite ribbons were surrounding larger iron nanoparticules [23].

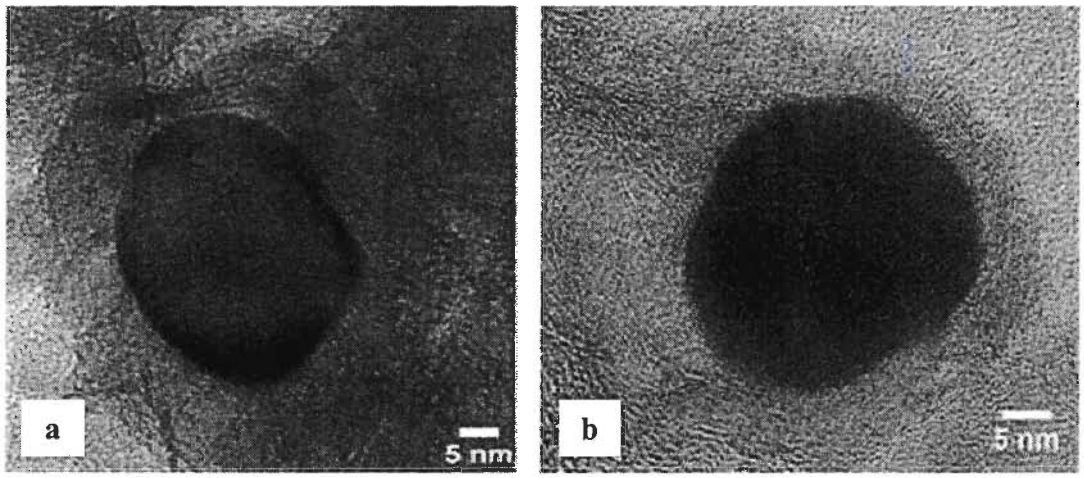

Figure 3.8: (a) and (b) TEM images of iron nanoparticules surrounded by graphite layers.

In Figure 3.9(a) we can see the presence of nanographite ribbons and amorphous carbon agglomerates with of diameter 90-100 nm and 120 nm, respectively. Figure 3.9(b) is the magnification of the image in the rectangle of Figure 3.9(a), where we see that amorphous carbon agglomerates on the left and a nanographite ribbon on the right.

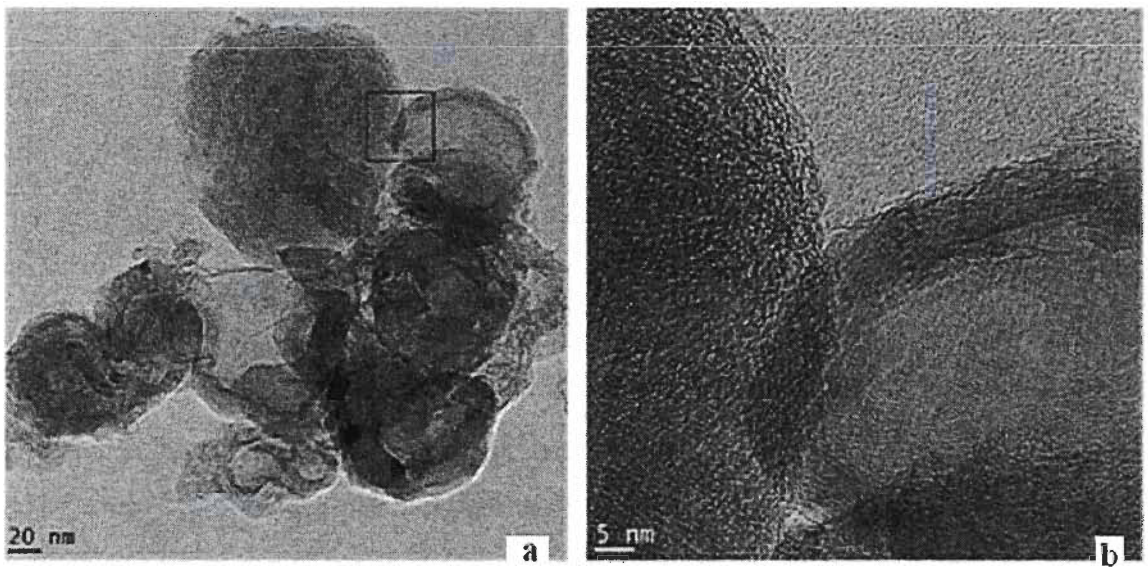

Figure 3.9: (a) TEM images of nanographite ribbons and amorphous carbon. (b) Magnification of the image in the rectangle of (a).

3.2.2 SPEX milled sample

Figure 3.10 is a TEM image of a purified SPEX sample (milled and heated). The image shows ribbon-like carbon nanostructures with curved diameter ranging from 40 to 130 nm and amorphous carbon agglomerates. Some metal nanoparticules (of about 20 nm in diameter) are also visible.

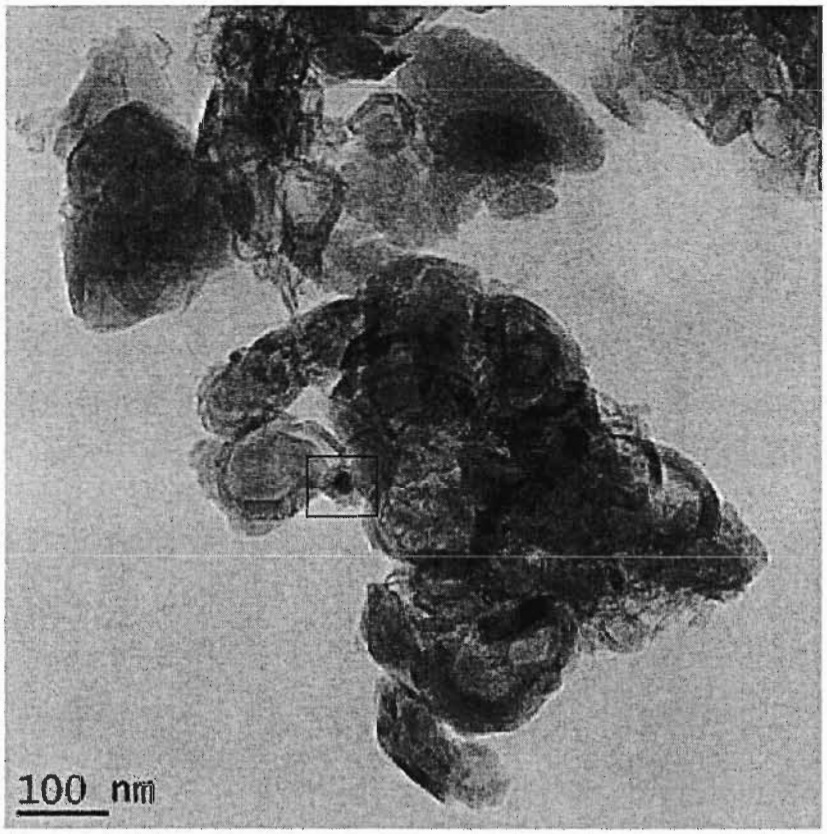

Figure 3.10: TEM image of a purified SPEX sample (milled for 12 h and heated at 700 °C for 90 minutes). We observe an iron particle (21 nm in diameter) surrounded by layers of graphite (image portion in the box)

From the TEM image of Figure 3.11(a) we can again see the formation of nanographite ribbons. Figure 3.11(b) is the magnification of the image in the rectangle of Figure 3.11(a), where the thicknesses of the nanographite ribbons are ranging from 3 to 10 nm and their diameters are ranging from 80 to 84 nm. Figure 3.12(a) shows nanographite ribbons where the thicknesses are ranging from 5 to 13 nm. Figure 3.12(b) is the magnification of the image in the rectangle of Figure 3.12(a) and shows a highly ordered graphitic structure with

thickness of about 8 nm. The distance between graphitic layers (d_{200}) is similar to Figure 3.6(b).

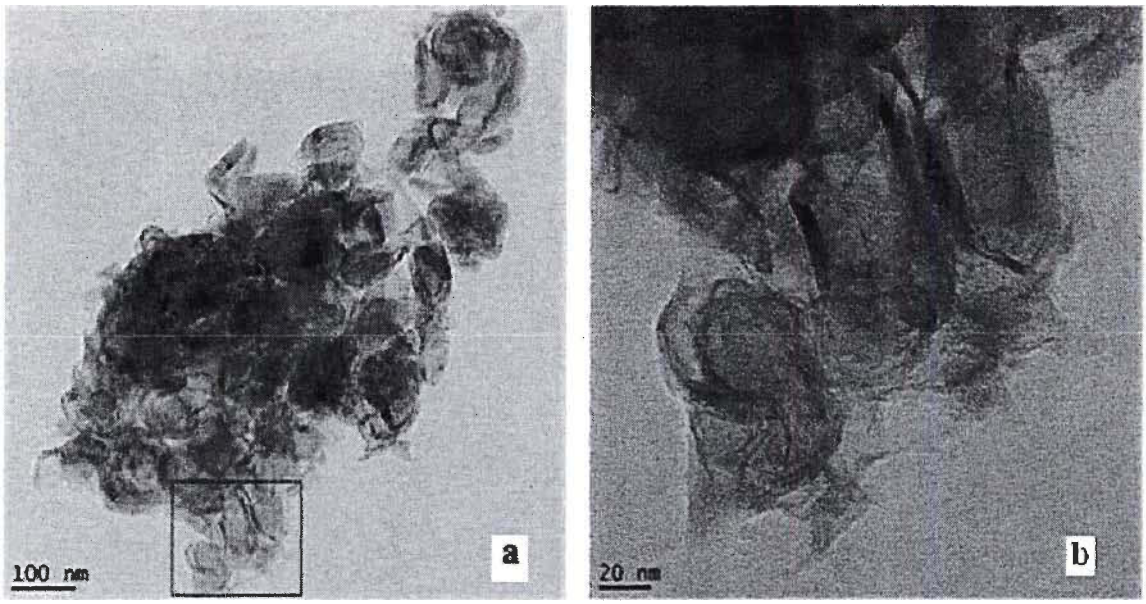

Figure 3.11: (a) TEM images of a purified SPEX sample (milled for 12 h and heated for 1 h at 700 °C). (b) Magnification of the image portion in the box of (a).

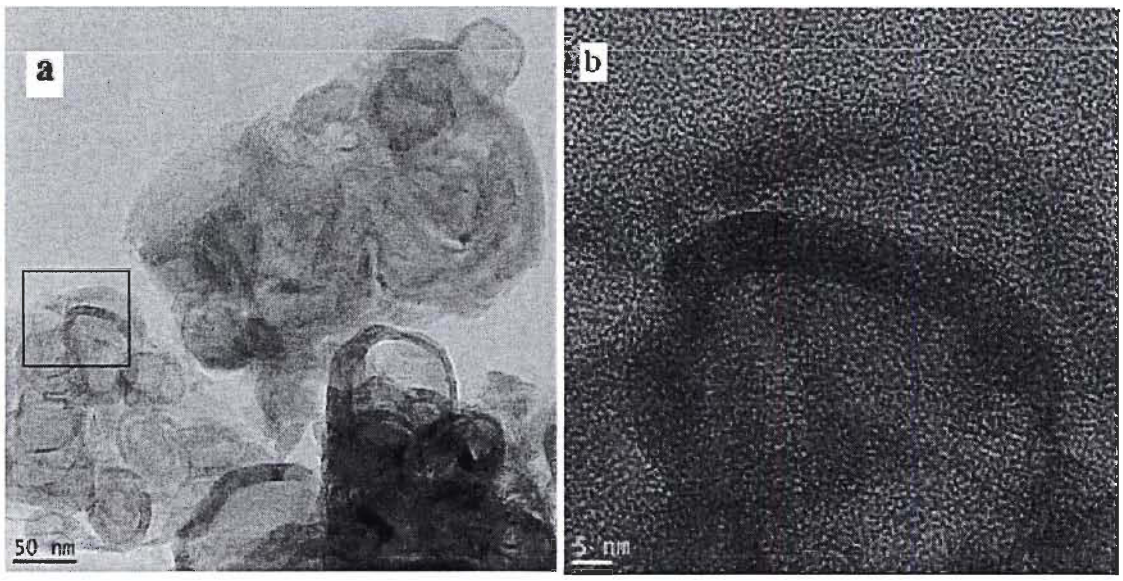

Figure 3.12: (a) TEM images of a purified SPEX sample (milled for 12 h and heated for 1 h at 700 °C). (b) Magnification of the image portion in the rectangle of (a).

Figure 3.13(a) shows a big doughnut shape carbon structure 92-110 nm in diameter. In the rectangle of Figure 3.13(b) we observe iron particles 20-30 nm in diameter surrounded by

graphite shells with an overall thickness of 9-13 nm. Figure 3.13(c) shows nanographite ribbons and amorphous carbon (square box) across an area of approximately 50 nm. Figure 3.13(d) is a magnification of the square box of Figure 3.13(c).

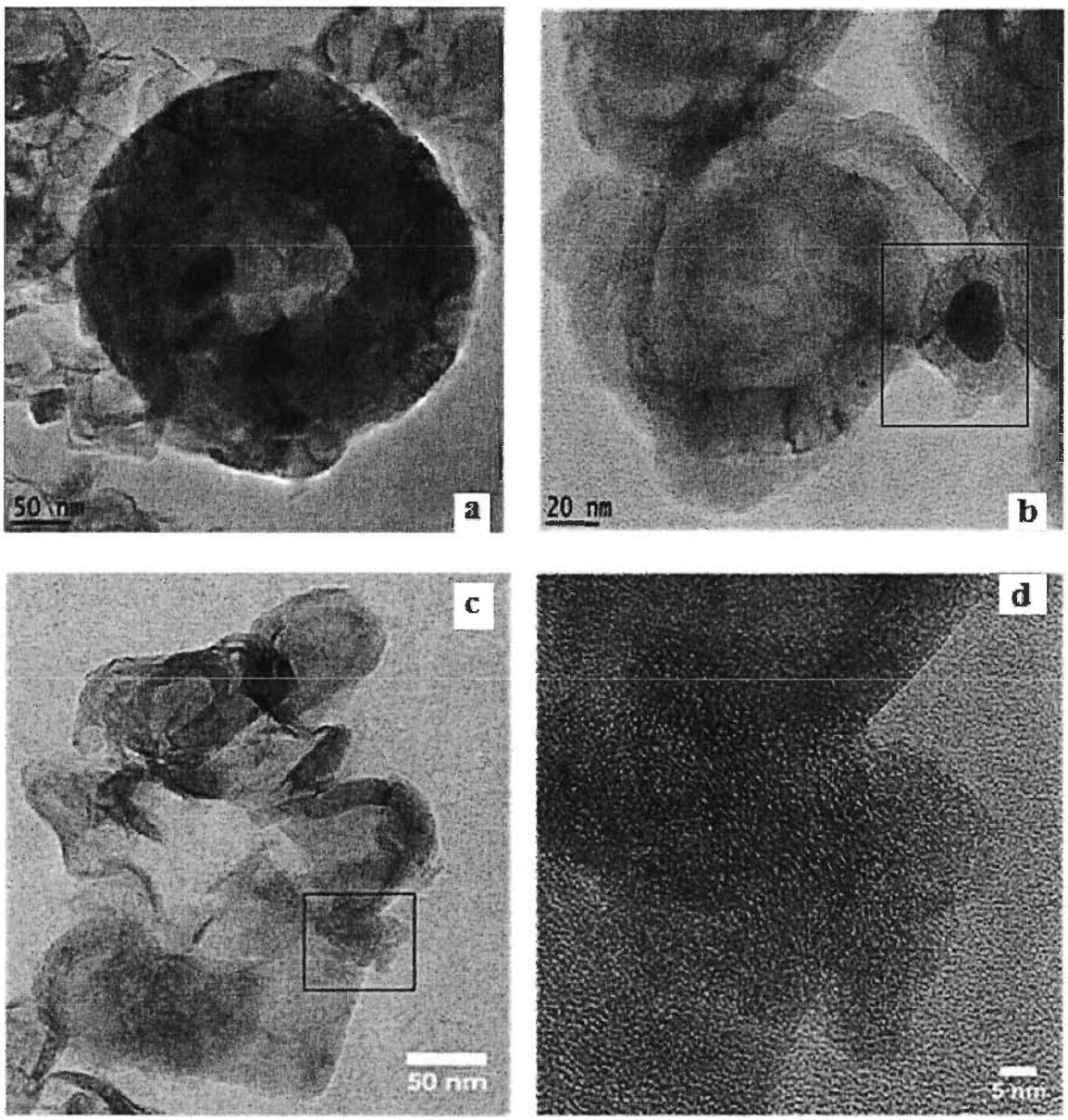

Figure 3.13: (a) TEM image of unique doughnut shaped carbon nanoribbon. (b) Iron particle surrounded by layers of graphite. (c) Nanographite ribbons with amorphous carbon. (d) Magnification of the image portion in the rectangle in (c).

3.3 Raman spectroscopy

Raman spectroscopy is used to characterize the structure of a wide variety of carbon materials like soot, carbon black and graphite. Raman spectroscopy can be used to characterize highly ordered materials with crystal structure as well as disordered materials because it is sensitive to the molecular structure (short-range order). In this work, we use Raman spectroscopy in the visible range and consider the first-order spectrum having frequencies less than 1,700 cm^{-1} and the second-order spectrum between 2,200 and 3,500 cm^{-1}. Figure 3.14 shows Raman spectra for activated carbon (used as a raw material), a SPEX milled sample (12 h) and a planetary milled sample (24 h) (both with iron and cobalt). In the planetary milled sample, we observe the presence of small peaks in the range 200-800 cm^{-1}. These peaks indicate the presence of fullerenic carbons (Fullerene has a graphite-like structure but instead of hexagonal packing it contains pentagonal structures). There are two important peaks in the first-order spectrum; the first one is the D band at about 1,300 cm^{-1} and is characteristic of disordered graphitic carbon with defects. The second one is the G band at about 1,580 cm^{-1} and corresponds to the graphitic lattice vibration mode with a E_{2g} symmetry due to vibrations of sp^2 bonds in hexagonal aromatic molecules of graphitic carbon.

In Figure 3.14, the position of the D band for activated carbon is centered at 1,360 cm^{-1}, 1,333 cm^{-1} for the SPEX milled sample, and 1,355 cm^{-1} for the planetary milled sample. The average in plane-length (L_a) of activated carbon is 2 nm. The broader D band of the planetary milled sample indicates a smaller size of graphite carbon (< 2 nm) compared to activated carbon and SPEX milled sample.

The position of the G band for activated carbon is centered at 1,595 cm^{-1}, 1,601 cm^{-1} for the SPEX milled sample, and 1,596 cm^{-1} for the planetary milled sample. The peaks are similar, indicating a similar graphitic structure for both samples.

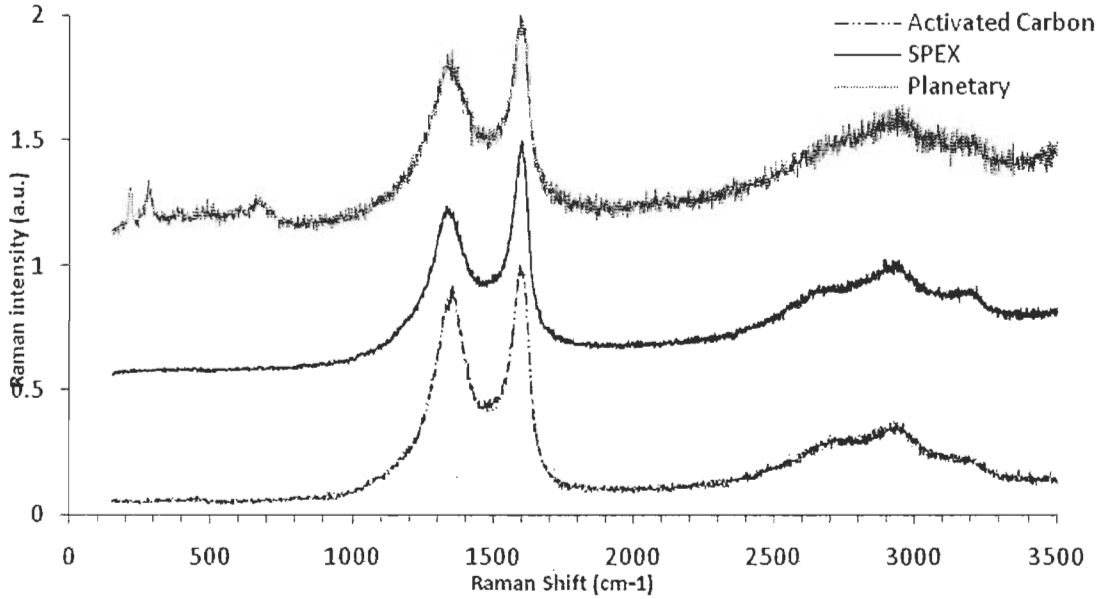

Figure 3.14: Raman spectra of activated carbon, SPEX milled sample (12 h), and planetary milled sample (24 h).

Figure 3.15 shows Raman spectra for a SPEX and a planetary milled sample after heating for 90 minutes under argon at 700 °C. We observe the appearance in the second-order Raman spectrum of the 2D band centered at about 2,700 cm^{-1}, which is a characteristic feature of highly ordered graphitic lattices [24]. After heating, the peaks corresponding to the G, D and 2D bands are sharper and have different positions than before heating (Table 3.1). The sharpness and decreasing widths of peaks corresponding to the D and G bands indicate that the carbon becomes more ordered after heating.

Raman spectra of purified SPEX and planetary samples in Figure 3.16 indicate that purification by hydrochloric acid for 3 h does not damage the graphitic structure and reduces the amount of amorphous carbon. The presence of amorphous carbon is represented by the height of the D_3 band centered at about 1,500 cm^{-1} (between the D and G peaks) [18, 24]. This reduction is indicated by the decrease in height of the D_3 band after purification.

Table 3.1 lists the values of the G, D and 2D bands before and after heating, and after purification by HCl.

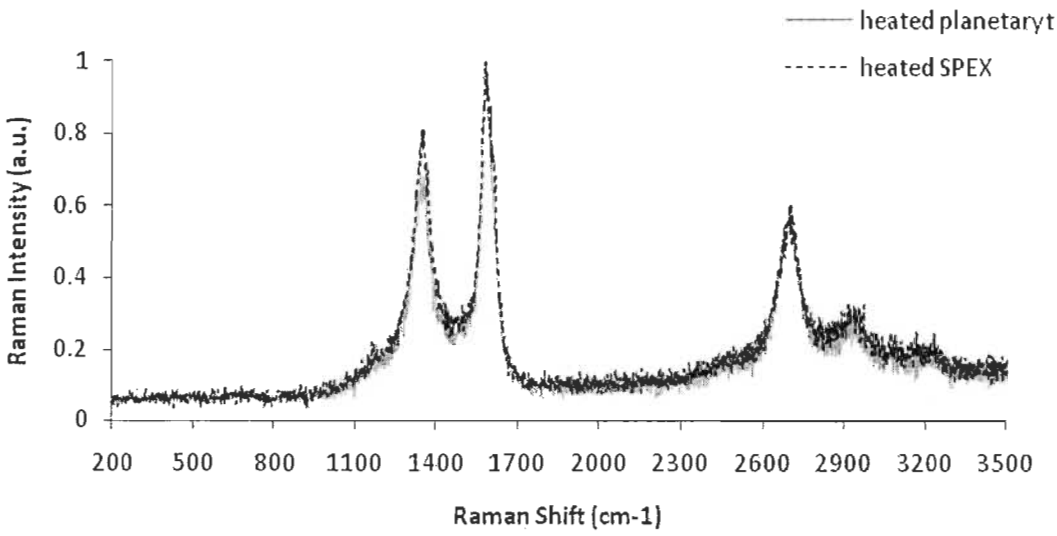

Figure 3.15: Raman spectra of a SPEX and a planetary sample after heating for 1.5 h at 700 °C.

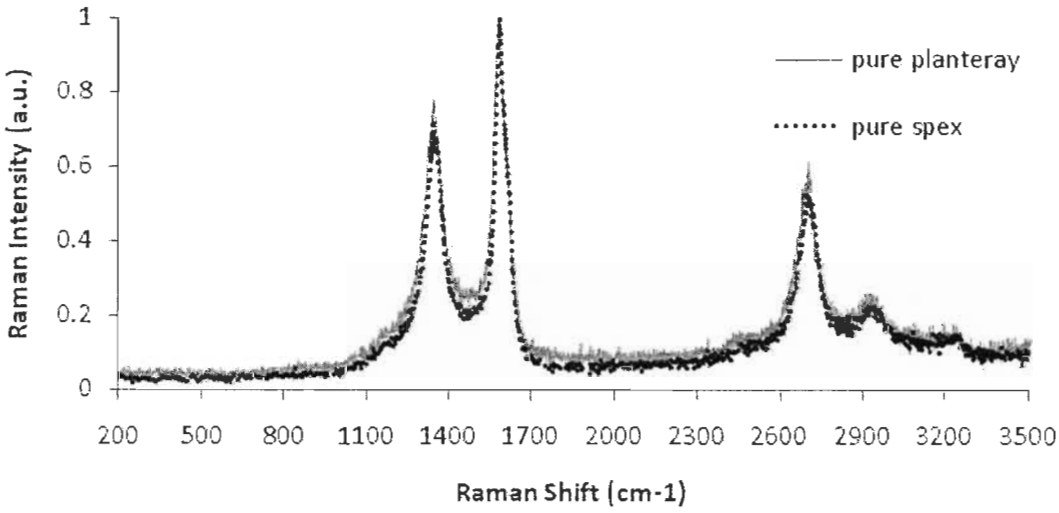

Figure 3.16: Raman spectra of a SPEX and a planetary sample after purification in HCl for 3 h.

Table 3.1: D, G, and 2D band positions of Raman spectra for SPEX and planetary samples.

	Samples	Raman peak position (cm^{-1}) [2]		
		D-band	G-band	2D-band
Raw material	Activated carbon	1,360	1,595	-
After milling	SPEX	1,333	1,601	-
	Planetary	1,355	1,596	-
After heating	SPEX	1,352	1,580	2,702
	Planetary	1,350	1,582	2,697
After purification	SPEX	1,343	1,582	2,702
	Planetary	1,344	1,577	2,696

Larouche and Stansfield [25] have proposed a new classification of carbon nanostructures (CNS) using graphitic indices derived from Raman spectra. Due to the presence of curvature in carbon graphite layers, the length of curved graphene planes (L_{eq}) is considered instead of straight in-plane length (L_a). L_{eq} is written as follow:

$$L_{eq} = 8.8 \left(\frac{A_{2D}}{A_D}\right),$$

where A_{2D} and A_D are the area of the 2D and D bands.

Figure 3.17 is a modified graph from Larouche and Stansfield [25] where our results have been added that shows the classification of various CNS as a function of two graphitization index, L_{eq} and $\Delta\omega_{2D}^{-1}$ (inverse of the full width at half maximum (FWHM) of 2D band) [18, 26]. According to Figure 3.17, SPEX and planetary samples have greater degrees of graphitization (greater values of L_{eq} and $\Delta\omega_{2D}^{-1}$) as compared to most of CNS.

[2] The precision of instrument is ± 1 cm^{-1}.

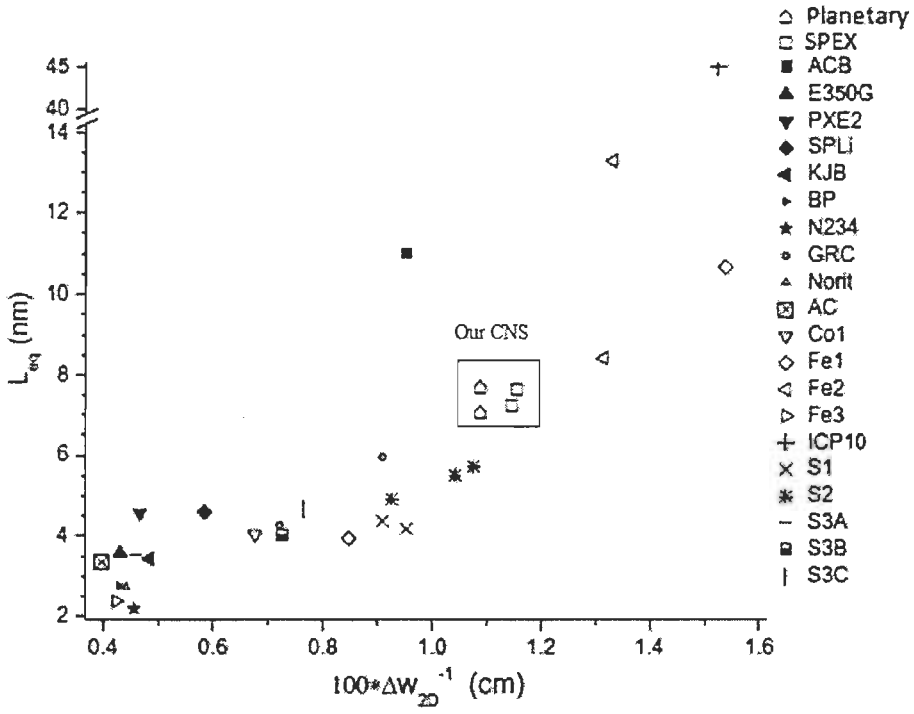

Figure 3.17: Classification of CNS using L_{eq} as a function of $\Delta\omega_{2D}^{-1}$ from reference [25] with SPEX and planetary samples.

3.4 N_2 adsorption isotherm

N_2 adsorption isotherm at 77 K is a technique to measure surface area, pore volume and pore size distribution. According to IUPAC, pore diameters are classified in three categories: micropores (< 2 nm), mesopores (2-50 nm) and macropores (> 50 nm). The total surface area is given by BET (Brunauer, Emmett, and Teller) analysis. The external and micropore surface area and the pore volume are given by t-Plot analysis.

Before measurement, samples were heated at 300°C for 24 h in vacuum. Table 3.2 lists the results for SPEX and planetary samples. Comparing the two samples indicates that planetary sample has a larger BET [27] and external surface area than the SPEX sample, while the micropore surface area of the SPEX sample is more than twice the value of the planetary

sample. The micropore volume of the SPEX sample is slightly larger than the micropore volume of the planetary sample.

Table 3.2: BET surface area, external and micropore surface area and volume by t-Plot analysis [31] for pure SPEX and planetary samples.

	BET specific surface area m^2/g	External surface area m^2/g (t-Plot)	Micropore surface area m^2/g (t-Plot)	Micropore volume cm^3/g (t-Plot)
SPEX	157.3	144.8	12.5	0.007
Planetary	197.3	192	5.3	0.0046

Figure 3.18 shows the N_2 adsorption and desorption isotherms for the purified SPEX and planetary samples. The isotherms are of type IV and indicate that the adsorption hysteresis behavior in the P/P_0 range from around 0.4 to 0.99 is mainly mesoporous [27]. The type IV isotherms indicate that slit-shaped pores are present in ribbon-like carbon nanoparticules, which may be derived from the interspaces of nanoparticules and their surface gaps [23].

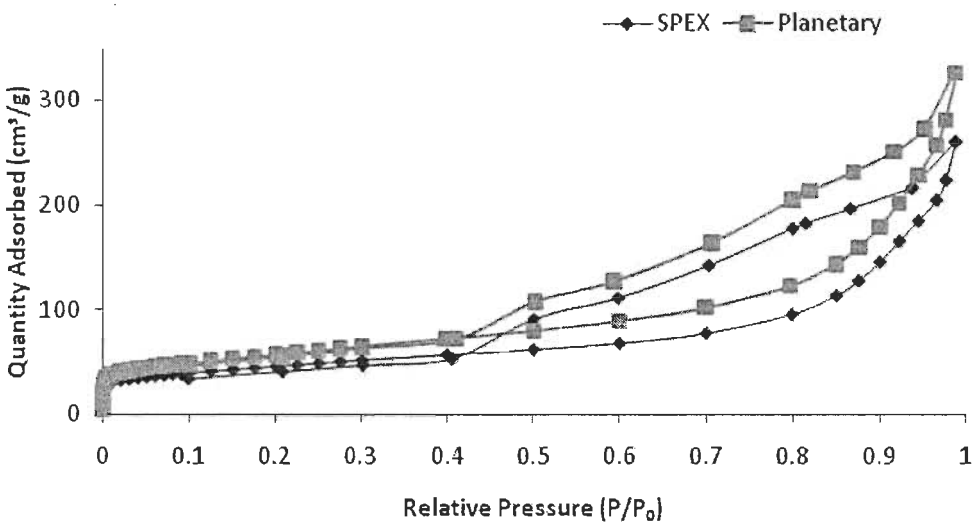

Figure 3.18: N_2 adsorption and desorption isotherms for purified SPEX and planetary samples.

Figure 3.19 shows the cumulative pore volume (desorption) as a function of pore dimension for mesopores ranging from 3 to 50 nm for SPEX and planetary samples, calculated using the BJH (Barrett, Joyner, and Halenda) method. According to Figure 3.19, the planetary sample has a larger mesopore volume than the SPEX sample.

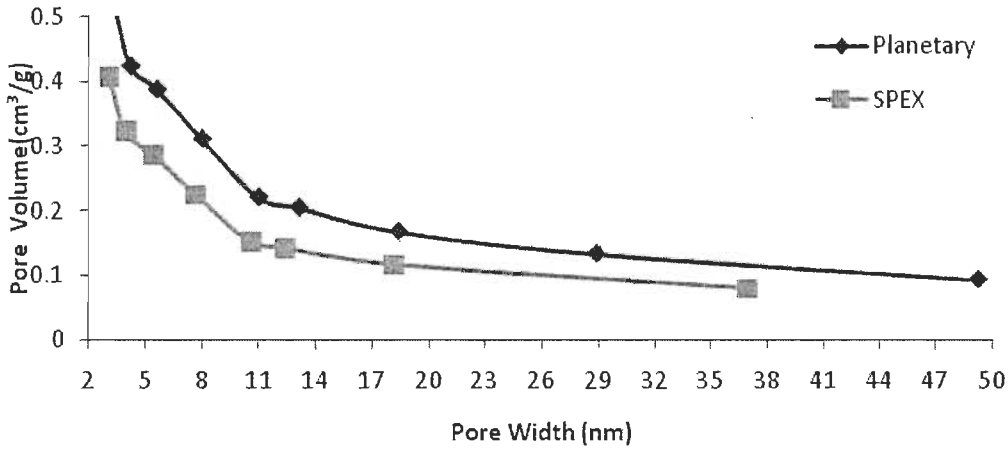

Figure 3.19: BJH cumulative pore volume (desorption) as a function of pore size for purified SPEX and planetary samples.

DFT (Density Functional Theory) [32] method uses the experimental isotherm data to determine both the mesoporosity and the macroporosity as a continuous distribution of the cumulative pore volume with respect to pore dimensions. Figure 3.20 shows a larger cumulative meso/macropore volume for the planetary sample. Consequently, the planetary sample has a larger mesopore and macropore volume than the SPEX sample. By contrast, the micropore volume of the SPEX sample is slightly larger than the planetary sample.

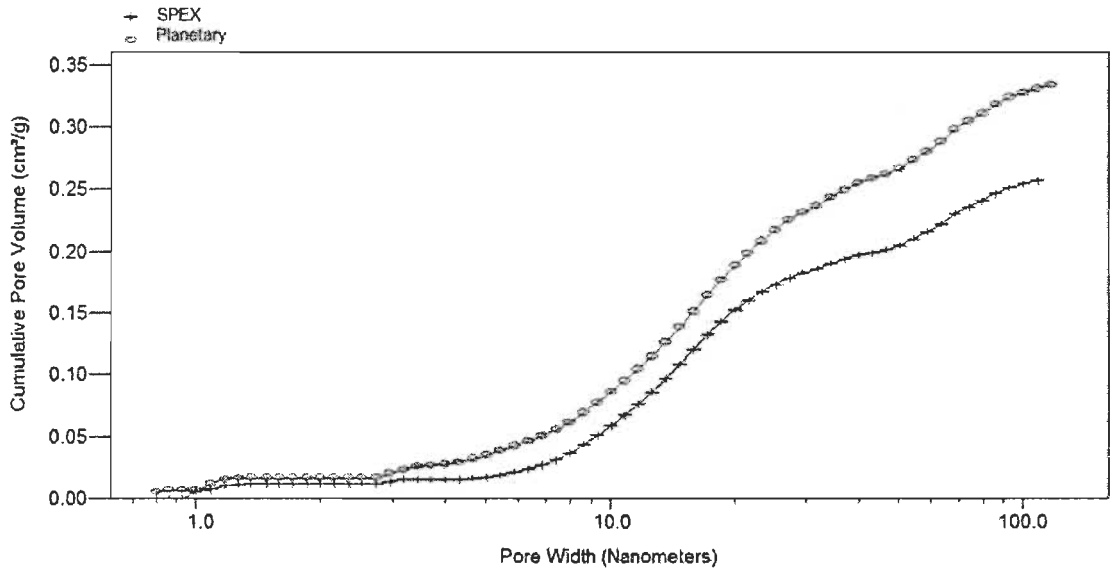

Figure 3.20: DFT distribution of cumulative pore volume of meso/macropores for purified SPEX and planetary samples.

3.5 Hg intrusion

The Hg intrusion data analysis determines the meso/macropore volume of CNS as a function of pore dimensions. Mesopore radius range from 0.001 to 0.025 μm and macropore radius are > 0.025 μm. Figure 3.21 shows the meso/macropore volume as a function of pore radius for SPEX and planetary samples. The curve of the SPEX sample on Figure 3.21 has one distinct peak at a pore radius of about 1 μm corresponding to a macropore volume of 160 mm^3/g. The curve of the planetary sample has two distinct peaks at about 0.1 and 1μm corresponding to macropore volumes of 40 and 80 mm^3/g, respectively. For the sake of comparison, data for Vulcan XC-72 (turbostratic carbon) from Passalacqua *et al.* [28] are also plotted on Figure 3.21. If we compare the peaks at 1 μm from our samples, with the main peak of Vulcan XC-72 at 5.5 μm, this shift in pore radius partly accounts for the higher pore volume found in our samples. The higher pore volume of our milled samples is attributed to the spacing between the CNS.

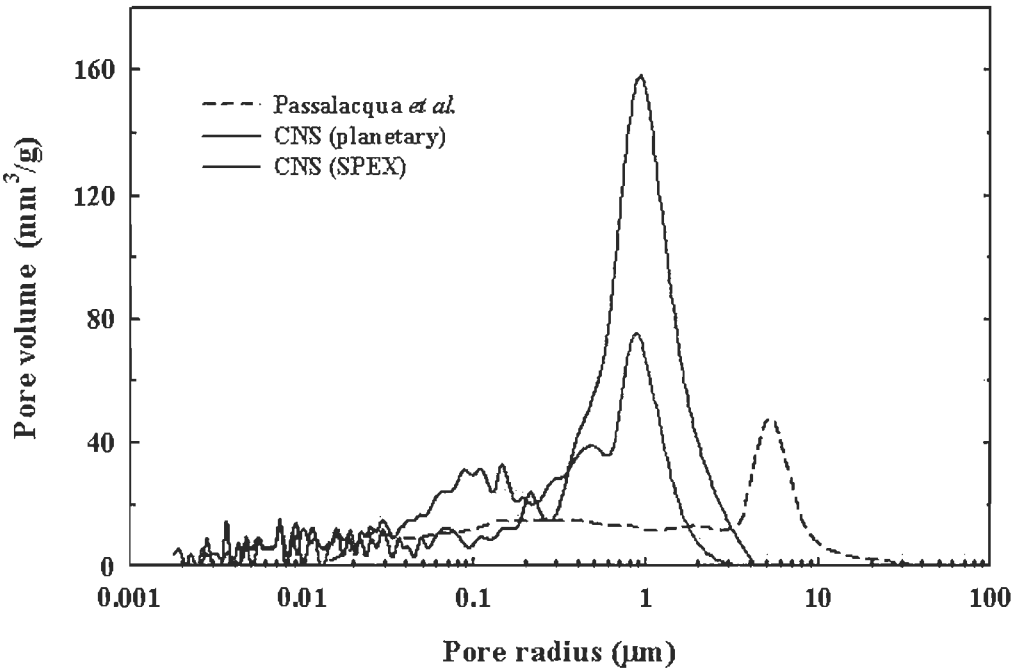

Figure 3.21: Macropore volume distribution from Hg intrusion data for SPEX and planetary samples, along with data from ref. [28] for Vulcan XC-72.

3.6 Thermal gravimetric analysis (TGA)

The purified SPEX and planetary samples were first prepared by heating them under argon atmosphere at 920 °C for 1 h .Figure 3.22 shows TGA data of purified SPEX and planetary samples with a common decomposition temperature centered at 660 °C. Since the oxidation temperature is relatively high, we can imply a high graphitization degree in our samples. Moreover, the TGA smooth curve of our samples is a proof of their high purity.

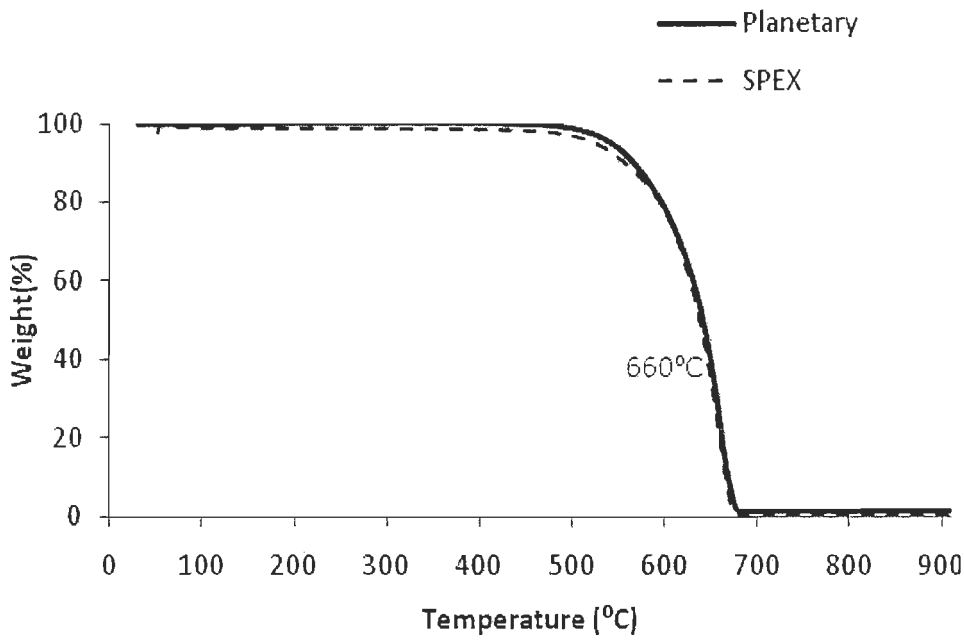

Figure 3.22: TGA analysis results under air atmosphere for SPEX and planetary samples.

Conclusions

We have presented a method to produce highly graphitized carbon nanostructures by ball milling of activated carbon with transition metals in the presence of hydrogen, followed by heating initially under argon. We have used two different mills, SPEX (high energy ball milling) for 12 h and planetary (low energy ball milling) for 24 h. We have analyzed and compared both samples after purification in HCl.

- TEM images show similar carbon nanostructures in both SPEX and planetary samples. The nanostructures are ribbon-like and horseshoe-like carbon nanoparticules with well-ordered graphitic layers and some defects. Both samples contain some amorphous carbon and iron nanoparticules (27-40 nm in diameter) surrounded by graphite layers. The thickness of ribbons ranges from 5 to 24 nm.
- X-ray diffraction patterns indicate that both SPEX and planetary samples are basically the same after heating and purification. The only minor differences are in crystallite sizes and interplanar spaces. The larger crystallite size and smaller interplanar layer d_{002} of the SPEX sample results in higher degree of graphitization.
- BET analysis shows that the total surface area for the SPEX sample is 157 m^2/g and 197 m^2/g for the planetary sample.
- N_2 adsorption isotherms indicate that the micropore volume for SPEX (0.007 cm^3/g) is almost twice the one of the planetary samples (0.0046 cm^3/g).
- N_2 adsorption and desorption isotherms show that both CNS samples are mainly meso/macroporous. BJH desorption and DFT confirm that the meso/macropore volume of the planetary sample is larger than the SPEX sample.
- Hg intrusion data analysis shows a macropore distribution with a single peak at 1 μm for the SPEX sample and with 2 peaks at 0.1 μm and 1 μm for the planetary sample.
- Raman spectra from the heated and purified SPEX and planetary samples are very similar. According to Raman classification proposed in ref. [25], our CNS can be compared very well with other carbon having a high degree of graphitization.

- TGA indicates that both SPEX and planetary samples have the same oxidation temperature centered at 660 °C and that they have a high purity.

From the results of this study we conclude that CNS produced by SPEX and planetary mills followed by heating and purification under the same conditions gives similar carbon nanostructures, although the SPEX sample has a higher degree of graphitization and a larger micropore volume. Ribbon-like carbon nanostructures could be good candidates as a catalyst support for PEMFC since it has meso/macroporous structure that could facilitate catalyst distribution, gas transportation and water managing.

Appendix I: Initial results

We prepared a sample named BM270208 by mixing CNS201 activated carbon 50 wt.%, iron 44 wt.% and cobalt 6 wt.% in a crucible and SPEX mill for 12 h under hydrogen atmosphere at 1.4 MPa. Figure I.1 shows the XRD pattern of sample BM270208 after heating at 700 °C for 1.5 h under argon. The formation of a cementite phase or Fe_3C during heating is observed.

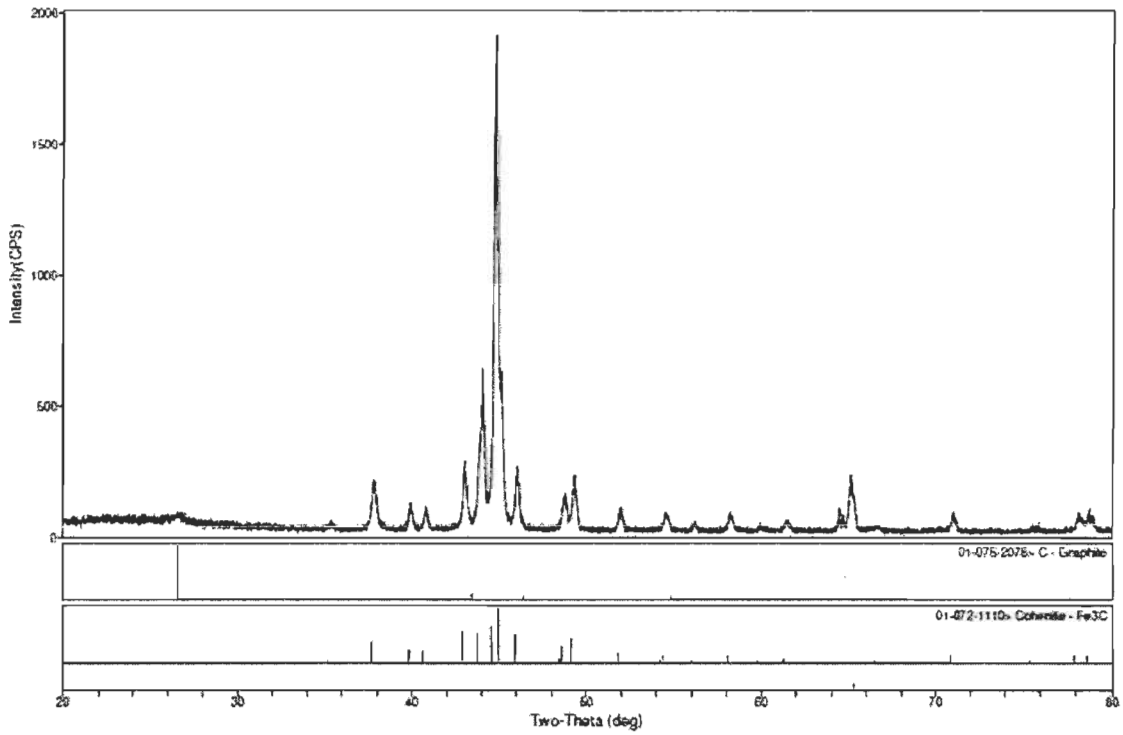

Figure I.1: XRD pattern of ball milled sample BM270208 after heating at 700 °C for 1.5 h under argon.

The purification of the heated sample to remove metal nanoparticules and amorphous carbon was done by putting back 500mg from the sample into H_2SO_4/HNO_3 (3:1) for 3 h at 120 °C. Figure I.2 shows the XRD pattern of purified sample BM270208. We observe the formation of crystalline graphite (002) at $2\theta \approx 26^\circ$ and iron reflections at $2\theta \approx 44.6^\circ$ and 65° with pilling related to (110) and (200), respectively. The XRD pattern of purified sample BM270208 in H_2SO_4/HNO_3 demonstrates that during the purification process, Fe_3C decomposes to iron and carbon graphite, although we expected iron to be completely removed.

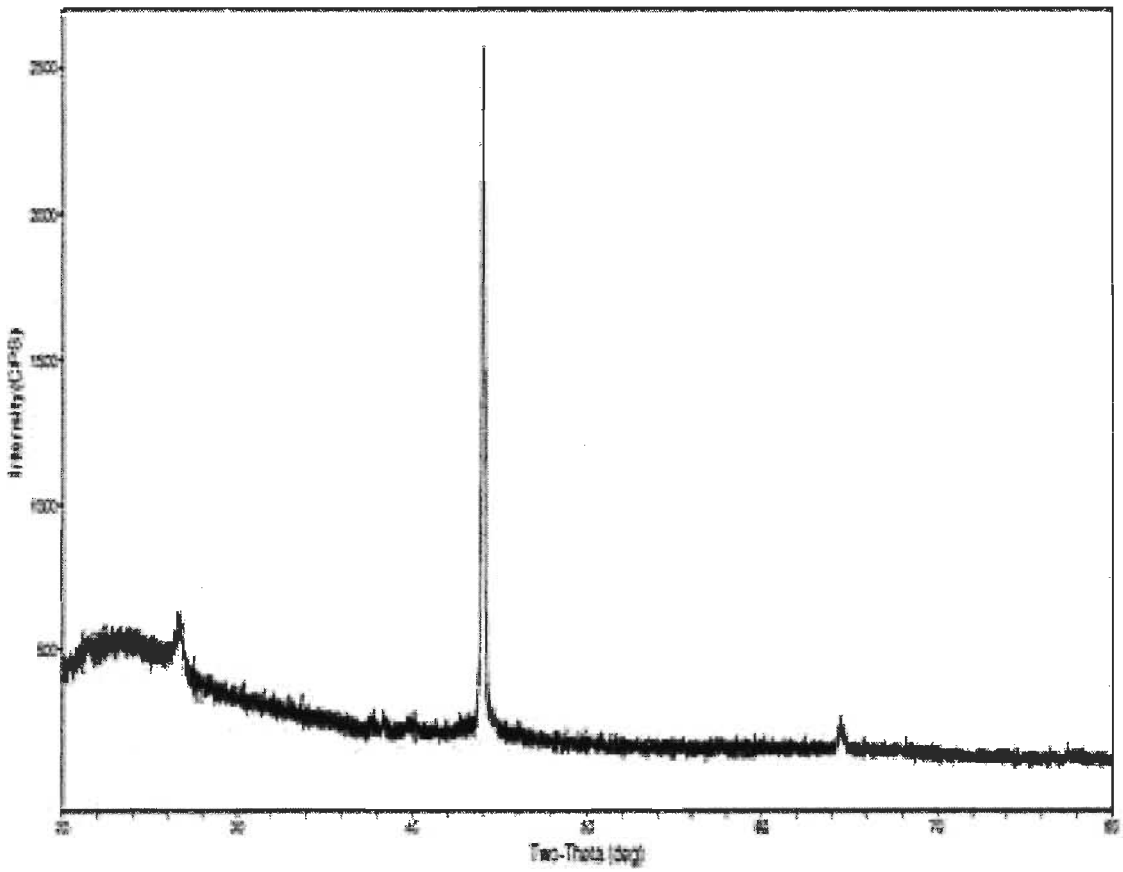

Figure I.2: XRD pattern of sample BM270208 after purification with H_2SO_4/HNO_3 for 3 h at 120 °C.

Another method of purification is to stir the sample in hydroclorydric acid (HCl) for 1 h instead of using a mixture of H_2SO_4/HNO_3. Figure I.3 shows the XRD pattern using this purification method, but we were not able to remove the metal impurities as iron peaks remained.

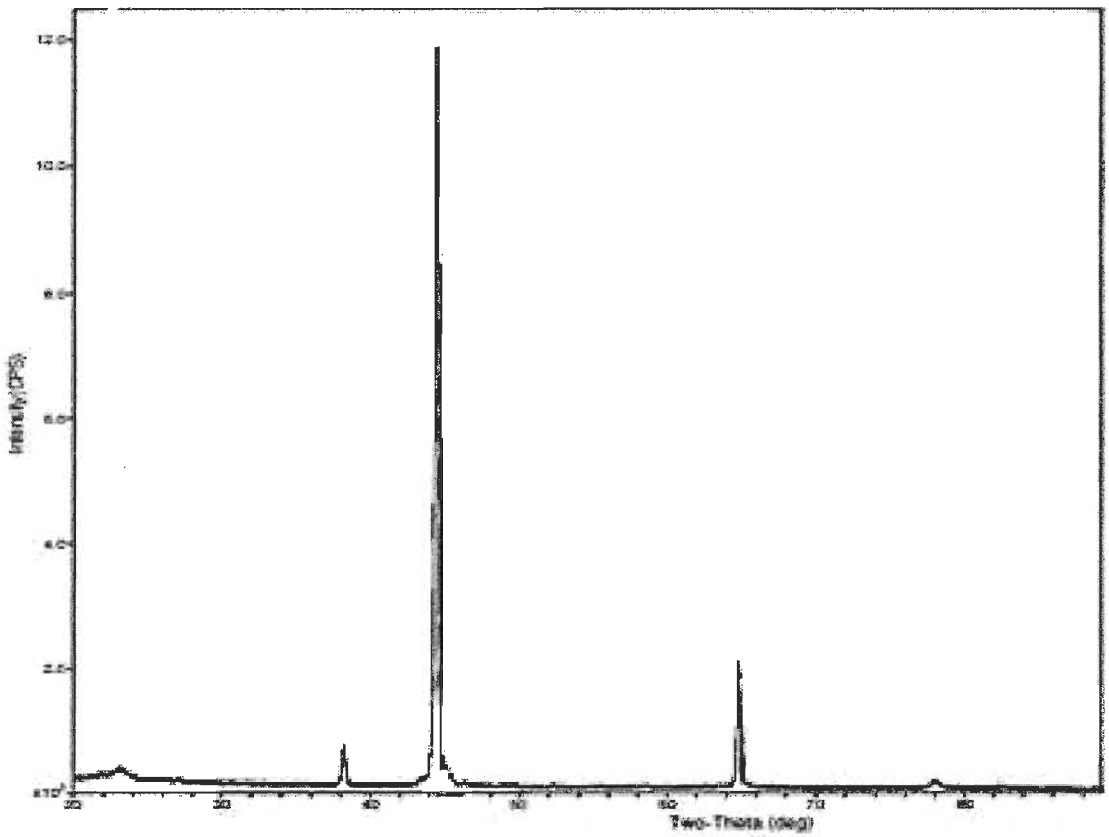

Figure I.3: XRD patterns of sample BM270208 after stirring with HCl for 1 h.

The Raman spectrum of milled sample BM270208 after heating and purification in HCl is shown in Figure I.4. The spectrum is similar to graphitic carbon black or activated carbon of Figure 3.14. The difference is in the D and G bands that are narrower.

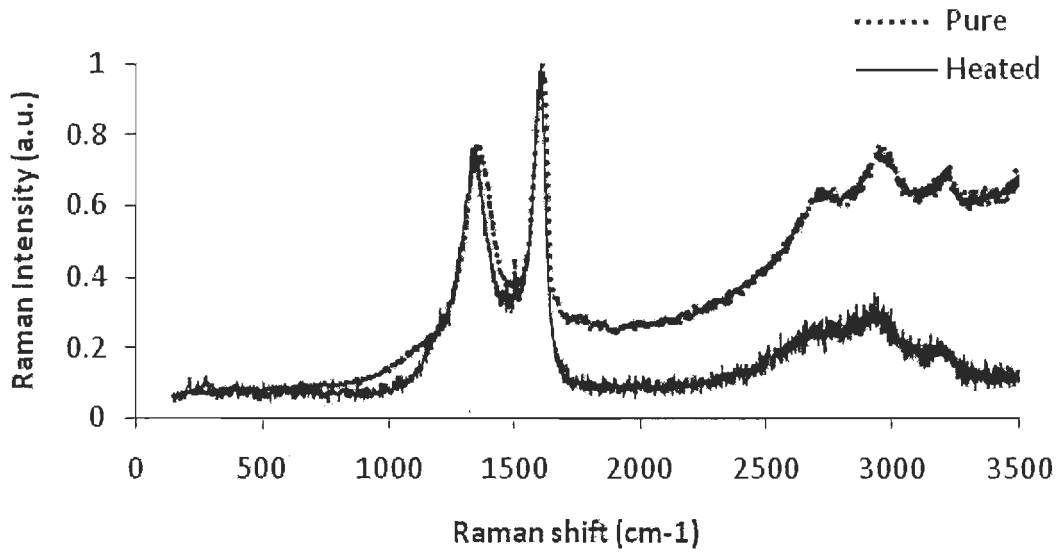

Figure I.4: Raman spectrum for milled sample BM270208 after heating and purification in HCl.

We find out that purification is more efficient if before acid chemical attack, an air oxidation for 24 h at 220 °C is applied. It was observed that the sonication of air oxidized carbon in 6 M HCl for 3 h placed in an ultrasonic bath can efficiently remove the impurities, but the surface area and porosity of the sample are not favorable. Air oxidation can increase the amount of surface oxygen-containing functional groups like carboxylic acids and quinines. XRD pattern of pure CNS for milled sample BM190309 is shown in Figure I.5(a). The sharp peak at $2\theta=26.19°$ corresponds to carbon graphite and there is no evidence of Fe peaks. Figure I.5(b) is the Raman spectrum of sample BM190309 and shows the appearance of 2D peak attributed to highly-ordered graphitic lattices.

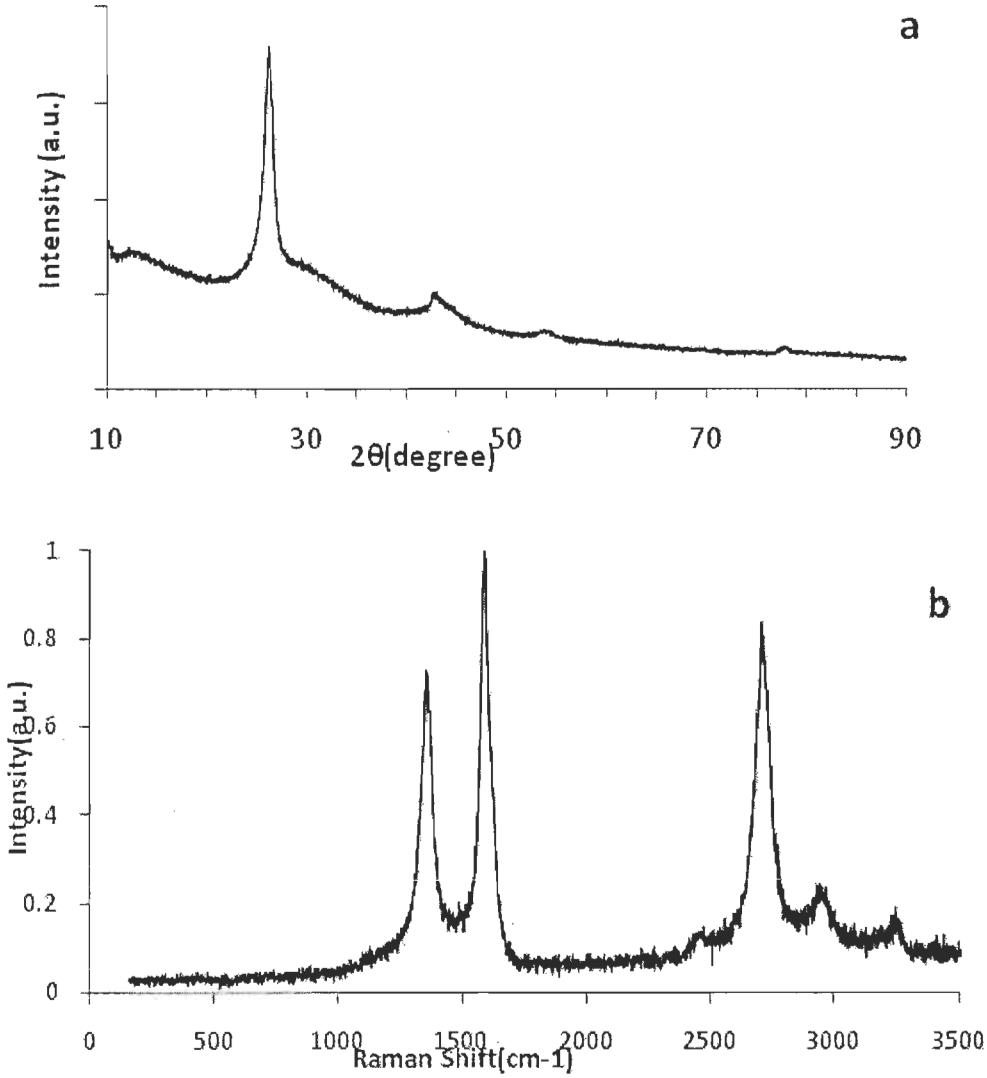

Figure I.5: (a) XRD pattern of sample BM190309 with air oxidation and purification in HCl. **(b)** Raman spectrum of the same sample.

Table I.1 summarizes purification methods and conditions of purification. Method #1 and #2 did not succeed to remove impurities while method #3 was efficient. Method #4 was effective after using new raw materials (results presented in Chapter 3).

Table I.1: Methods of purification of CNS.

#	Purification methods	Molarity	Time (h)	Temperature (°C)	Result
1	Refluxing in H_2SO_4/HNO_3	3:1	3	120	×
2	Stirring in HCl	12	1	23	×
3	Oxidation in air Sonication in HCl	- 6	24 3	220 40	√
4	Sonication in HCl	6	3	40	Chapter 3

Table I.2 lists the surface area and micropore volume of a sample after SPEX ball milling and heating under argon for 90 min, followed by purification with method #3. We observed that after milling a high surface area CNS201 (~ 1200 m^2/g) with iron and cobalt, the micropore surface area decreased to 128 m^2/g. After heating, micropores were destroyed; however, macro and mesopore surface area increased due to crystallization of milled sample and decomposition of iron carbide to iron and CNS. Purification with HCl increases meso and macropore surface area (two times more than heating) and creates a micropore surface area. Moreover, it has been shown that purification by hydrofluoric acid (HF) also increases micropore, mesopore and macropore surface area and volume more than other acids [29].

Our XRD results show that CNS and iron carbide (Fe_3C) are formed during the heating stage. In a previous paper, Natarajan *et al.* [2] have found that the addition of Co in the milling stage prevents the formation of Fe_3C and purification methods #1 and 2 remove impurities. So, it is important to find out the reason of Fe_3C formation. A possible cause of presence of Fe_3C in samples BM270208 and BM190309 can be due to contamination. Indeed, that was the cause since samples made with new raw materials (Fe and Co) did not show traces of Fe_3C (see Appendix II).

Table I.2: BET surface area, micro and external surface area and micropore volume for BM190309 after ball milling, heating and purification by method #3.

	Total surface (m^2/g) BET	Micropore surface area (m^2/g) t-Plot	External surface area (m^2/g)	Micropore volume (cm^3/g) t-Plot
Ball milling	156.02	128.03	27.98	0.051
Heating	55.09	*	57.48	-0.0018
Purification	128.01	15.35	112.65	0.0075

Appendix II: Contamination

A serious problem with the milling of fine powders is the potential for significant contamination especially from milling tools (crucible and balls) and starting powder. In this section we verify how to reduce these kinds of contamination for our samples.

Milling tools

One of the most common contaminations during milling of powder is Fe element from the crucible and balls since they are made from hardened steel. During ball milling, the balls impact onto the powder, the crucible and onto each other. The powder particles are not only cold welded with themselves but also with the milling tools under high energy collision. The cold welded powder will finally be fractured from the balls and crucible by direct collision [15]. All these effects can contaminate the powder with iron. The extent of contamination increases by increasing milling energy, use of higher BPR, higher speed of milling and long milling duration [14].

We supposed that the large quantity of Fe comes from attrition of the wall of the steel crucible used for ball milling. We have purchased another crucible body and machined the lid to obtain a smooth surface, but we still had the presence of Fe_3C in our samples.

Eskandarany *et al.* [30] found out that a thin coating on the internal surface of crucible or balls with the material to be milled will minimize contamination. The idea is to mill the powder once, allowing the powder to be coated on milling tools. Then, the milled powder is discarded and new powder is milled but with the old crucible and balls; crucible and balls should not be cleaned. If milling is repeated several times, the contamination should be minimized. We have used coating three times, but we still had the presence of Fe_3C in our samples.

Another technique to reduce contamination from grinding medium is to use rod milling instead of spherical balls. In a conventional ball mill, the impact forces scratch surface of the milling media and debris from the milling media and contaminate the powder being milled.

On the other hand, if shear forces dominate, they are more effective in kneading the powder mixtures and final powder is much less contaminated. To achieve this minimized contamination, the balls were replaced by long rods rotating in a cylindrical vial exert shear forces on the material [14].

Starting powder

Starting materials such as activated carbon, iron and cobalt have great importance and should be proper to get desired result in experiments. Powders with high surface area have much tendency to absorb nitrogen, oxygen and water vapor. So, to remove gas adsorbed on activated carbon surface, it was heated under vacuum at 1,000 °C for 1 h. To prevent air contamination, Fe and Co are maintained in glove box under argon atmosphere. In addition, it is advised to choose the proper type of powder and if possible coarser powder.

When we considered the expiration date on the iron and cobalt bottles, it was revealed that the products had expired. Therefore, by purchasing new iron and cobalt, the problem of iron carbide formation was solved.

Appendix III: Supplemental results

After heating a planetary milled sample, it was further milled for 1 h and 2 h in a SPEX and then purified by HCl. The sample milled for 1 h is BM#1 and the sample milled for 2 h is BM#2. The XRD patterns of Figure III.1 shows a broad graphite peak.

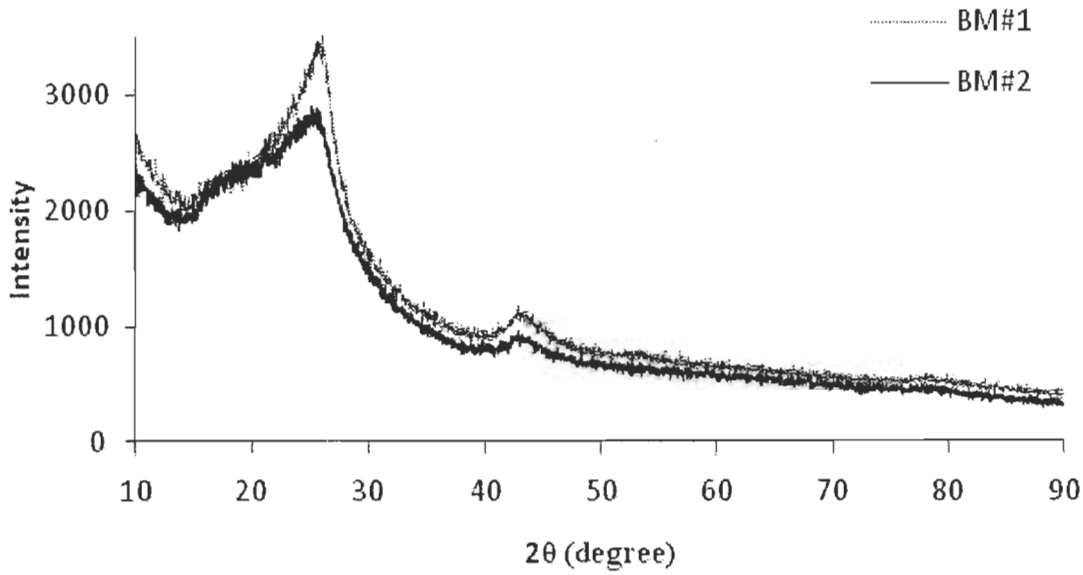

Figure III.1: XRD patterns for samples BM#1 and BM#2.

N_2 adsorption isotherm measurement for BM#1 shows that compared to planetary and SPEX surface area in Table III.1,the micropore surface area increases significantly up to 150 m^2/g. Higher BET surface area and micropore volume are observed.

Table III.1: N_2 adsorption isotherm measurement for BM#1.

	BET m^2/g	External surface area m^2/g (t-Plot)	Micropore surface area (m^2/g) t-Plot	Micropore volume (cm^3/g) t-Plot
BM#1	351.7	201	150.6	0.063

References

[1] Barbir F, "PEM fuel cells: theory and practice", *New York: Elsevier Academic Press* (2005).

[2] Jiujung zhang, "PEM fuel cell electrocatalysts and catalyst layer fundamental and application", *Springer* (2008).

[3] Larminie J, Dicks A, "Fuel cell systems explained", Chicester, *England: John Wiley and Sons* (2003).

[4] Feng-Yuan Zhang, Dusan Spernjak, Ajay K. Prasad, and Suresh G. Advani , "In Situ Characterization of the Catalyst Layer in a Polymer Electrolyte Membrane Fuel Cell", *Journal of the Electrochemical Society* ,154(11), pp.B1152-B1157 (2007).

[5] S.K. Natarajan, D. Cossement and J. Hamelin, "Synthesis and Characterization of Carbon Nanostructures as Catalyst Support for PEMFCs", *Journal of the Electrochemical Society* 154(3), pp. B310-B315 (2007).

[6] S.K. Natarajan and J. Hamelin, "Homogeneous Pt Deposition on Chemically Modified Carbon Nanostructures as Catalysts for PEMFCs", *Electrochimica Acta* 52(11), pp. 3741-3757 (2007).

[7] S.K. Natarajan and Jean Hamelin, "Electrochemical Durability of Carbon Nanostructures as Catalyst Support for PEMFCs", *Journal of the Electrochemical Society*, 156(2), pp. B210-B215 (2009).

[8] Rupesh Khare, Suryasarathi Bose, "Carbon Nanotube Based Composites- A Review", *Journal of Minerals & Materials Characterization & Engineering*, 4(1), pp. 31-46 (2005)

[9] Fu Liu, Xiaobin Zhang, Jipeng Cheng, Jiangpin Tu,Fanzhi Kong,Wanzhen Huang, Changpin Chen, "Preparation of short carbon nanotubes by mechanical ball milling and their hydrogen adsorption behavior", *Carbon*, 41(13), pp.2527–2532 (2003).

[10] Craig P. Marshall and Michael A. Wilson,"Ball milling and annealing graphite in the presence of cobalt", *Carbon*, 42(11), pp.2179–2186 (2004).

[11] B. Bokhonov and M. Korchagin, "The formation of graphite encapsulated metal nanoparticles during mechanical activation and annealing of soot with iron and nickel", *Journal of Alloys and Compounds*, 333(1-2), pp. 308–320 (2002)

[12] Thomas W.Ebbesen, "Carbon nanotubes:Preparation and Properties" , *NEC Research Institute Princeton*, New Jersy (1997).

[13] Siân Fogden, Raquel Verdejo, Ben Cottam, Milo Shaffer, "Purification of single walled carbon nanotubes: The problem with oxidation debris",*Chemical Physics Letters*, 460(1-3), pp. 162–167 (2008), The references there in [18,19].

[14] Suryanarayana.C, "Mechanical alloying and milling" , *NewYork: Marcel Dekker* (2004).

[15] Li Lu,Man On Lai, " Mechanical alloying" ,*USA .Kluwer academic publishers* (1998).

[16] Melanie Francke, Helmut Hermann, Roswitha Wenzel, Gotthard Seifert, Klaus Wetzig "Modification of carbon nanostructures by high energy ball-milling under argon and hydrogen atmosphere",*Carbon*, 43(6), pp.1204–1212 (2005).

[17] Wang Y, Alsmeyer DC, McCreery RL, "Raman spectroscopy of carbon materials: structural basis of observed spectra", *Chemistry of Materials*, 2(5), pp.557–563 (1990).

[18] Sadezky A, Muckenhuber H, Grothe H, Niessner R, Po¨ schl U,"Raman microspectroscopy of soot and related carbonaceous materials: spectral analysis and structural information", *Carbon*, 43(8), pp.1731–1742 (2005).

[19] Jean-Philippe Tessonnier *et al* . "Analysis of the structure and chemical properties of some commercial carbon nanostructures", *Carbon*, 47(7), pp.1779-1798 (2009).

[20] Ruslan Sergiienko , Etsuro Shibata, Sunghoon Kim, Takuya Kinota, Takashi Nakamura, "Nanographite structures formed during annealing of disordered carbon containing finely-dispersed carbon nanocapsules with iron carbide cores",*Carbon*,47(4),pp.1056-1065 (2009). The reference there in [32].

[21] Mildred.S.Dresselhause,Gene Dresselhause ,Phaedon Avouris (Eds), "Carbon nanotubes synthesis,structure,properties and applications" , *Springer* (2000).

[22] Hiroyuki Fujimoto, "Theoretical X-ray scattering intensity of carbons with turbostratic stacking and AB stacking structures", *Carbon*,41(8), pp. 1585–1592 (2003).

[23] Mu Zhao, Huaihe Song, Xiaohong Chen, Wentao Lian, "Large-scale synthesis of onion-like carbon nanoparticles by carbonization of phenolic resin", *Acta Materialia*, 55(18), pp. 6144–6150 (2007).

[24] A. Cuesta, P. Dhamelincourt, J. Laureyns, A. Martínez-Alonso, J.M.D. Tascón, "Raman microprobe studies on carbon materials", *Carbon*, 32(8), pp.1523-1532 (1994).

[25] Nicholas Larouche , Barry L. Stansfield, "Classifying nanostructured carbons using graphitic indices derived from Raman spectra", *Carbon*, 48(3), pp.620-629 (2010).

[26] P. Lespades and A. Marchand, "Caractérisation de matériaux carbonés par microspectrométrie Raman", *Carbon*, 22(4-5), pp. 375–385 (1984).

[27] Gregg S. J. , K. S. W. Sing, "Adsorption, surface area, and porosity". *New York: Academic Press* (1982).

[28] E. Passalacqua, G. Squadrito, F. Lufrano, A. Patti and L. Giorgi, "Effects of the diffusion layer characteristics on the performance of polymer electrolyte fuel cell electrodes", *Journal of Applied Electrochemistry*, 31(4), pp. 449–454 (2001).

[29] Lyubov Lafi , Daniel Cossement, Richard Chahine, " Raman spectroscopy and nitrogen vapour adsorption for the study of structural changes during purification of single-wall carbon nanotubes", *Carbon*, 43(7), pp.1347–1357 (2005).

[30] M.Sherif El-Eskandarany, "Mechanical alloying for fabrication of advanced engineering materials", *USA.William Andrew publishing* (2001).

[31] Sebastian Storck, Helmut Bretinger, Wilhelm F. Maier, "Characterization of micro- and mesoporous solids by physisorption methods and pore-size analysis", *Applied Catalysis A: General* ,174(1), pp.137-146 (1998).

[32] Alexander V. Neimark , Yangzheng Lin, Peter I. Ravikovitch, Matthias Thommes, "Quenched solid density functional theory and pore size analysis of micro-mesoporous carbons",*Carbon*,47(7), pp.1617-1628 (2009).